(12)

RADC-TR-87-22
Final Technical Report
February 1987

THEORETICAL DESIGN STUDY OF A 2-18 GHz BANDWIDTH HELIX TWT AMPLIFIER

University of Utah

Michael A. Frisoni

APPROVED FOR PUBLIC RELEASE; DISTRIBUTION UNLIMITED

ROME AIR DEVELOPMENT CENTER
Air Force Systems Command
Griffiss Air Force Base, NY 13441-5700

RADC-TR-87-22 has been reviewed and is approved for publication.

APPROVED: Andrew E Chrostowski

ANDREW E. CHROSTOWSKI, 1LT, USAF
Project Engineer

APPROVED: Frank J Rehm

FRANK J. REHM
Technical Director
Directorate of Surveillance

FOR THE COMMANDER: John A. Ritz

JOHN A. RITZ
Directorate of Plans & Programs

UNCLASSIFIED
SECURITY CLASSIFICATION OF THIS PAGE

[illegible]

REPORT DOCUMENTATION PAGE

Form Approved
OMB No. 0704-0188

1a. REPORT SECURITY CLASSIFICATION
UNCLASSIFIED

1b. RESTRICTIVE MARKINGS
N/A

2a. SECURITY CLASSIFICATION AUTHORITY
N/A

2b. DECLASSIFICATION / DOWNGRADING SCHEDULE
N/A

3. DISTRIBUTION / AVAILABILITY OF REPORT
Approved for public release; distribution unlimited.

4. PERFORMING ORGANIZATION REPORT NUMBER(S)
UTEC MD-86-059

5. MONITORING ORGANIZATION REPORT NUMBER(S)
RADC-TR-87-22

6a. NAME OF PERFORMING ORGANIZATION
University of Utah

6b. OFFICE SYMBOL *(If applicable)*

7a. NAME OF MONITORING ORGANIZATION
Rome Air Development Center (OCTP)

6c. ADDRESS *(City, State, and ZIP Code)*
Department of Electrical Engineering
Salt Lake City UT 84112

7b. ADDRESS *(City, State, and ZIP Code)*
Griffiss AFB NY 13441-5700

8a. NAME OF FUNDING / SPONSORING ORGANIZATION
AFOSR

8b. OFFICE SYMBOL *(If applicable)*
NE

9. PROCUREMENT INSTRUMENT IDENTIFICATION NUMBER
F30602-82-C-0161

8c. ADDRESS *(City, State, and ZIP Code)*
Bolling AFB
Wash DC 20332

10. SOURCE OF FUNDING NUMBERS

PROGRAM ELEMENT NO.	PROJECT NO.	TASK NO	WORK UNIT ACCESSION NO.
61102F	2305	J9	16

11. TITLE *(Include Security Classification)*
THEORETICAL DESIGN STUDY OF A 2-18 GHz BANDWIDTH HELIX TWT AMPLIFIER

12. PERSONAL AUTHOR(S)
Michael A. Frisoni

13a. TYPE OF REPORT	13b. TIME COVERED	14. DATE OF REPORT (Year, Month, Day)	15. PAGE COUNT
Final	FROM Sep 82 TO Oct 86	February 1987	104

16. SUPPLEMENTARY NOTATION
Research was accomplished in conjunction with Air Force Thermionics Engineering Research Program (AFTER) AFTER-18. Michael A. Frisoni was an AFTER student from Varian (See Reverse)

17. COSATI CODES

FIELD	GROUP	SUB-GROUP
09	03	

18. SUBJECT TERMS *(Continue on reverse if necessary and identify by block number)*
Helix Traveling Wave Tubes
Large Signal Analysis
Crestatron Interaction Phenomena
Computer Simulation

19. ABSTRACT *(Continue on reverse if necessary and identify by block number)*

This report investigates the concept of applying an extremely dispersive helix section prior to a nondispersive helix section in a traveling-wave tube (TWT) output circuit in order to realize a 2-18 GHz frequency bandwidth. The nondispersive helix circuit provides the synchronism for multioctave performance, and the dispersive helix circuit yields the second harmonic relative phase shift necessary for harmonic suppression at the low frequency band edge. Fundamental efficiency enhancement and harmonic power content are shown to be a function of the circuit phase velocity characteristics, the injection velocity parameter, and circuit length. Also described is the effect of the Crestatron interaction phenomena on the TWT's performance. All the results are based on one-dimensional large signal computer calculations.

20. DISTRIBUTION / AVAILABILITY OF ABSTRACT
☒ UNCLASSIFIED/UNLIMITED ☐ SAME AS RPT. ☐ DTIC USERS

21. ABSTRACT SECURITY CLASSIFICATION
UNCLASSIFIED

22a. NAME OF RESPONSIBLE INDIVIDUAL	22b. TELEPHONE (Include Area Code)	22c. OFFICE SYMBOL
Andrew E. Chrostowski	(315) 330-4381	RADC (OCTP)

DD Form 1473, JUN 86 *Previous editions are obsolete.*

SECURITY CLASSIFICATION OF THIS PAGE
UNCLASSIFIED

16. SUPPLEMENTARY NOTATION (Continued)

Associates. This report was submitted in partial fulfillment of the requirements of the degree of Electrical Engineer.

ACKNOWLEDGMENTS

This research was made possible by the joint sponsorship of the Air Force and Varian Associates in conjunction with the University of Utah under the Air Force Thermionic Engineering and Research (AFTER) program. The study was supervised by Dr. Richard W. Grow of the University of Utah, and Mike Cascone at Varian Associates. I would like to thank them, and also thank Dr. John Putz for the benefit of their discussions during the course of this work. The generous assistance of the Electrical Engineering Department secretaries at the University of Utah is also acknowledged.

TABLE OF CONTENTS

Page

LIST OF ILLUSTRATIONS AND TABLES

Tables

I. INTRODUCTION

In the area of microwave amplifiers, there is no other device which can match the traveling-wave tube's (TWT) combination of bandwidth and gain. The TWT has expanded into fields ranging from space exploration to electronic warfare to domestic communication systems. Many electronic countermeasure (ECM) systems require average power levels over extremely wide bandwidths which only the TWT can satisfy. In systems currently in use, the 2-18 GHz band is covered by 3 tubes. New systems will eventually cover this band with 2 tubes.

The main hindering problem in obtaining a 2-18 GHz bandwidth by a single TWT is degraded fundamental efficiency and an enhanced harmonic power content at low band frequencies. Due to the wide bandwidth and high gain, and plus the fact that the TWT acts as a nonlinear device when driven to saturation, harmonics will be generated and appear in the RF output spectrum. Typically, the second harmonic is the most dominant.

The purpose of this study is to numerically determine the conditions which enhance the fundamental efficiency and suppress second harmonic growth at the low band edge frequency $f = 2$ GHz, and to realize an output circuit design that achieves reasonable electronic efficiency across the entire 3.2 octave frequency band. All the results are based on large signal TWT computer simulations.

The organization of this report is as follows. Chapter 2 provides the historical background of the basic ultrabroadband (UBB) design concepts and summarizes the results of past analyses. Chapter 3 describes the approach used to define the circuit impedance as a function of the cold circuit velocity characteristics so that the dispersion can be arbitrarily shaped. Chapter 4 defines the large signal theory and assumptions used in this analysis. Chapter 5 discusses the numerical results which define the conditions necessary to achieve a 3.2 octave operating bandwidth. Chapter 6 presents a summary of the results and lists recommendations for further studies. Appendix A supports Chapter 3 and details an analysis used to verify an impedance assumption applied in the study. Appendix B defines a set of symbols commonly used throughout the paper. Appendix C explains the phase plots used in Chapter 5.

II. THE ULTRA-BROADBAND CONCEPT AND HISTORICAL PERSPECTIVE

There are several important considerations in the design of ultrabroadband traveling-wave tubes. The criteria to achieve multioctave performance was first outlined by Walchli[1] and later refined by Rymer and Cascone.[2] These conditions are as follows:

1. Velocity synchronism between the forward circuit wave on the helix and the slow space-charge wave of the beam must be sustained over the entire frequency band.
2. Harmonic generation must be suppressed.
3. The helix output circuit must be long enough to provide reasonable efficiency at all frequencies.
4. A method for suppressing backward-wave oscillation (BWO) must be implemented.
5. Excessive forward-wave gain and gain ripple must be minimized in order to eliminate in-band instability.

The scope of this paper is concerned with conditions 1, 2, and 3.

The fundamental concept in the design of an ultrabroadband TWT is a two-section output circuit, as shown schematically in Fig. la. The first section is an unloaded helix circuit which is positively dispersive. The second section is a loaded helix circuit which displays negative to flat dispersion. See Fig. lb.

In the past, "loading" the circuit in order to change the dispersion characteristics of a helix circuit was accomplished by placing a conducting shield near the helix by use of dielectric supports, or by extending radial metal vanes from the shield toward the helix.[3,4]

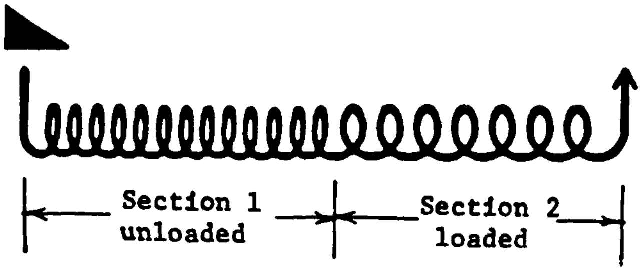

Fig. 1a. Schematic view of the output circuit.

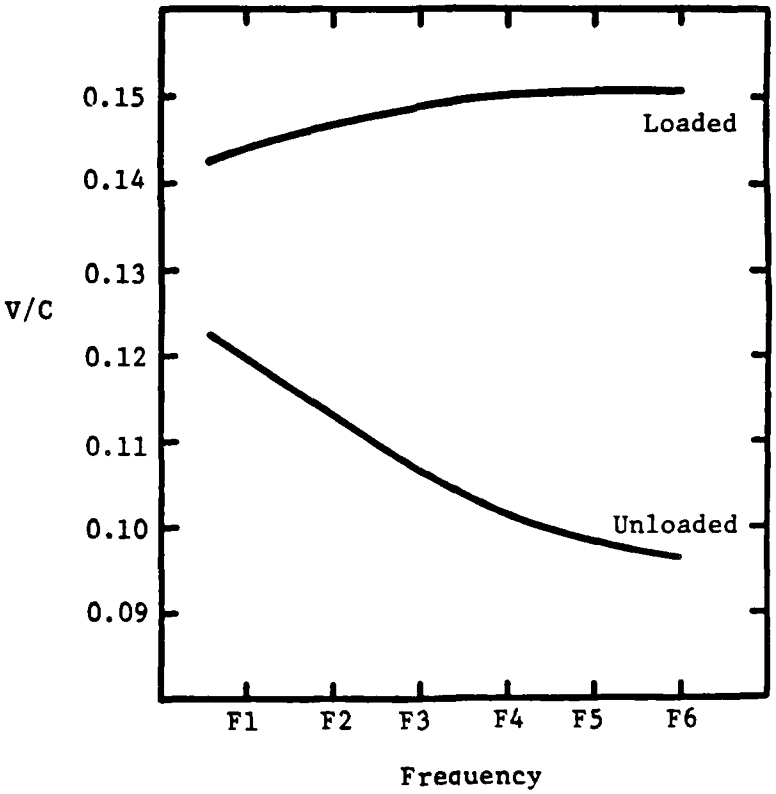

Fig. 1b. Phase velocity characteristics of loaded and unloaded helix circuit.

Advancements in phase velocity dispersion control have brought about the development of metal loading segments placed between the dielectric supports.[5] This technology allows the cold circuit dispersion to be shaped in order to optimize TWT design parameters (i.e., Pierce parameters b, C). Experimental results[6] have shown that the use of metal loading segments has improved a TWT's operation in terms of increased bandwidth, decreased gain variation, and decreased sensitivity to operating voltage.

The original design[7] of the two-section output circuit was such that the loaded helix section was optimized for efficiency at the middle and upper frequencies. It also provided some gain at the lower end of the band. The unloaded helix section was unsynchronized with the slow space-charge wave at all frequencies. It was predicted that the gain of this section would not result from the normal exponential growth of the forward circuit wave, but would occur due to a beating wave phenomenon called the Crestatron effect.

The Crestatron effect occurs when the injection velocity parameter "b" is greater than b for $x_1 = 0$ (in terms of Pierce TWT theory[8]). The three forward waves propagating on a RF structure are known to vary as $e^{-\Gamma z}$. The complete propagation constant is defined as

$$-\Gamma_i = \beta C x_i - j\beta \left(1 - C y_i\right)$$

where

β = wave phase constant

z = axial distance

C = gain parameter

x,y = incremental propagation constants

i = 1, 2, 3 represent the three waves

Figure 2 displays the incremental propagation constants versus the injection velocity and is used as an example to illustrate the relationship between x_1 and b. The figure indicates that at approximately $b = 1$, x_1 has reached a peak value so maximum exponential growth of the forward circuit wave occurs. As the injection velocity parameter increases in value, x_1 eventually converges to zero. At $b = 2.5$, $x_1 = 0$ and remains zero for $b > 2.5$. When $x_1 = 0$, the propagation constant of the forward circuit wave changes from a complex to a purely imaginary value, thus normal exponential growth does not occur. The gain produced is a result of the beating between the three forward waves. Interaction is primarily between the forward circuit wave and the slow space-charge wave. At certain points along the circuit, the phase relationship between the circuit RF field and the RF current in the beam is such that energy is transferred to the circuit, resulting in a region of positive gain. Conversely, there are other points along the tube where energy is transferred to the beam, resulting in a gain null. To utilize the efficiency of this phenomenon, the circuit must be terminated at a point where a positive gain peak occurs.

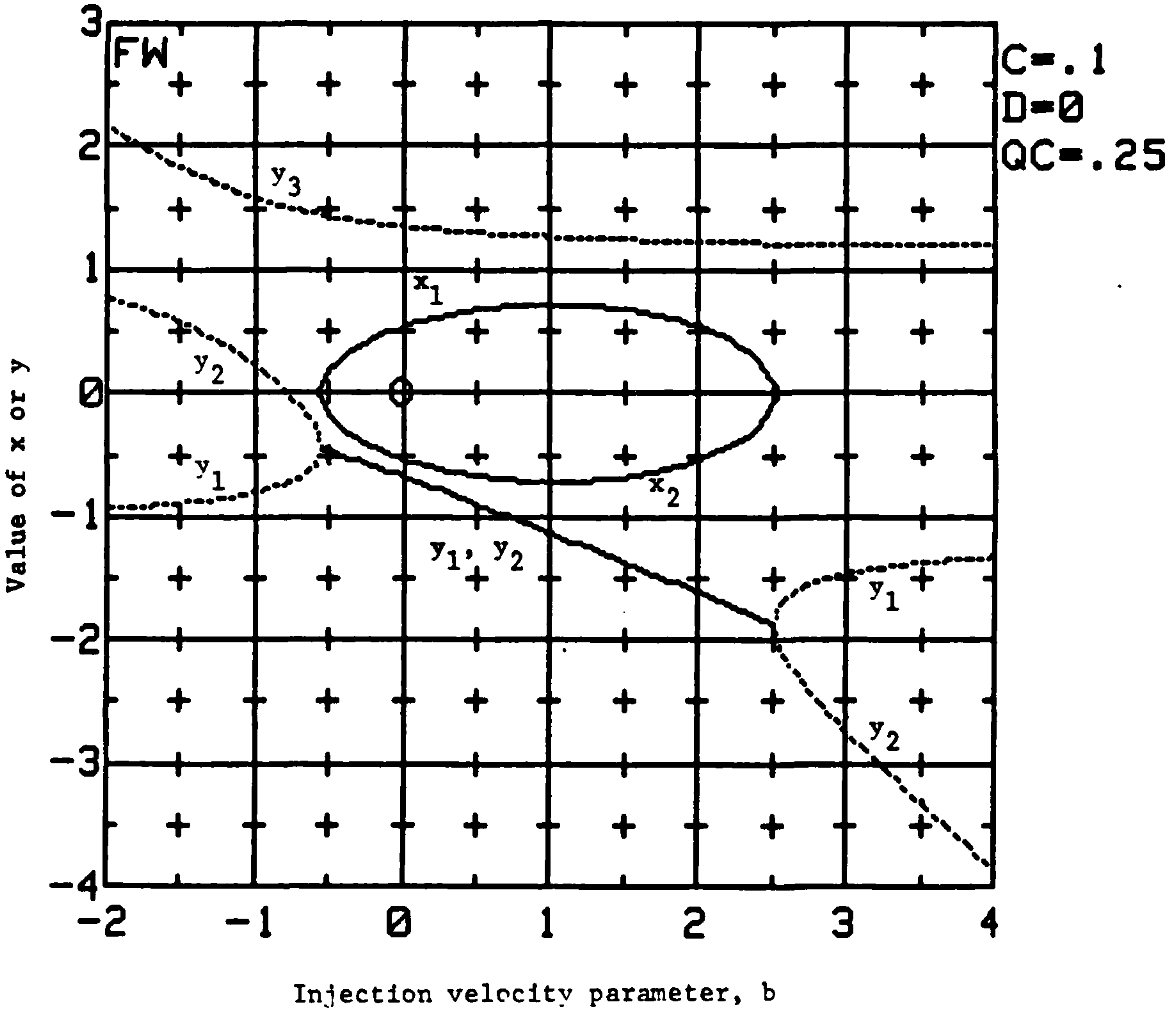

Fig. 2. Pierce incremental propagation constants versus the injection velocity parameter.

Figures 3a and 3b, obtained from a study published by Rowe,[9] illustrate the small and large signal characteristics of the Crestatron interaction phenomenon. Figure 3a illustrates the small signal gain fluctuation for numerous injection velocities. The figure also displays the normal exponential growth of the forward circuit wave (b = 1, 2, 2.5). It further indicates that as b increases, the gain decreases. Figure 3b displays the saturation efficiency as a function of the drive level for different values of b. The figure shows that the efficiency peaks at an input signal level dependent upon the value of b. As the injection velocity parameter increases, the input drive level must be increased in order to obtain maximum efficiency. The figure further illustrates that the Crestatron saturation point occurs at much higher drive levels than in the normal growing wave case (b = 1.5). It was also noted that the optimal length (i.e., for maximum output) changes as the drive level changes.

A traveling-wave tube, based on this two-section output circuit design, was built and found to achieve a bandwidth of 2.58 octaves (3-18 GHz). The bandwidth was limited due to an enhanced harmonic and a degraded fundamental performance at the lower band edge. The electronic efficiency varied between 5 and 12.5 percent. The dc beam current and voltage were 390 mA and 10.1 kV, respectively. The saturated output power versus frequency is shown in Fig. 4a.

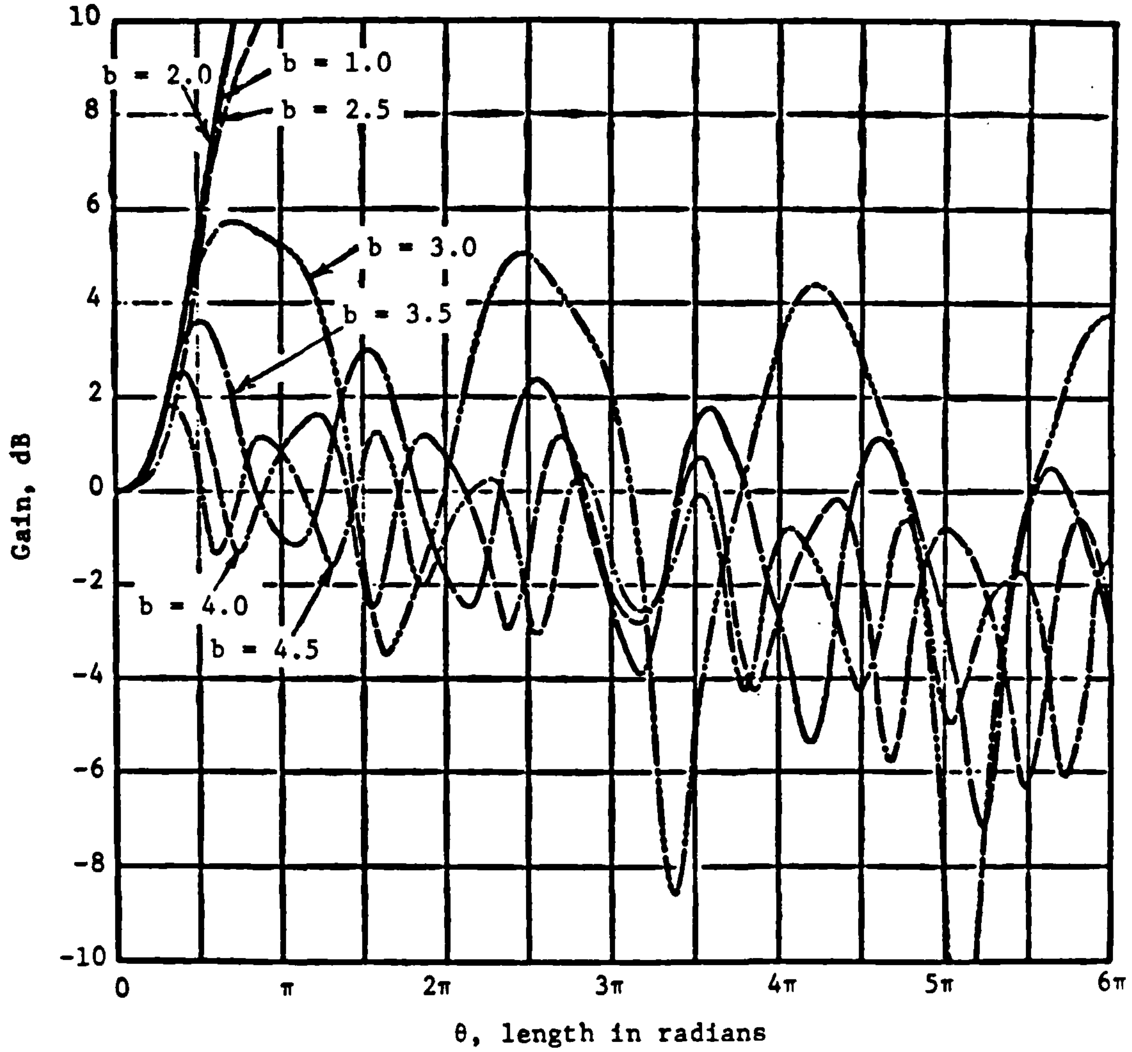

Fig. 3a. Crestatron gain versus length ($C = 0.2$, $QC = 0.125$, $d = 0.025$, $b_{x_1=0} > 3.0$).

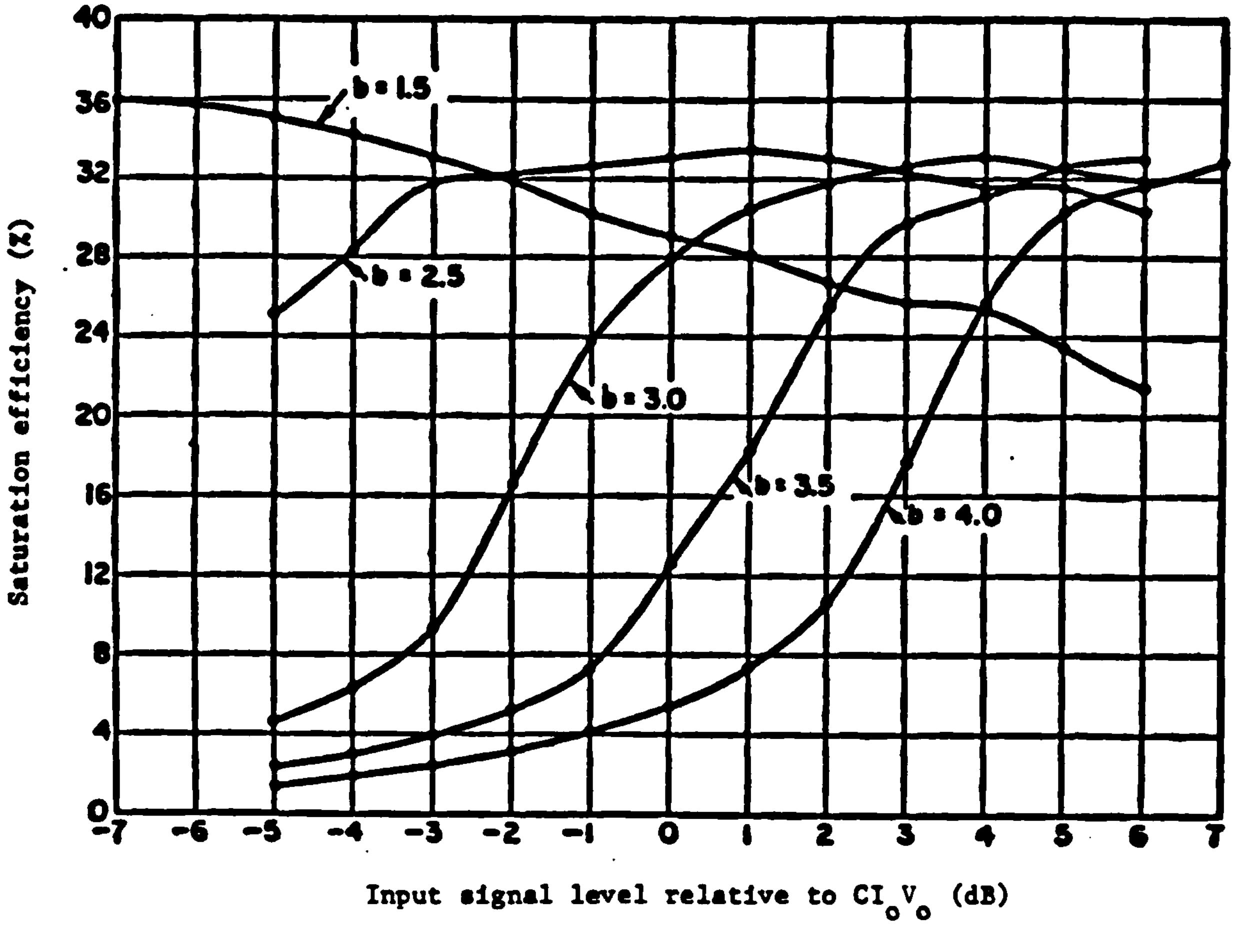

Fig. 3b. Crestatron theoretical saturation efficiency versus input-signal level with injection velocity as the parameter ($C = 0.1$, $QC = 0.125$, $d = 0$, $b_{x_1=0} = 2.33$).

The next design approach[2] was based upon the desire to further increase the operating bandwidth. The concept of a two-section output circuit was retained, but the relative phase velocities between the sections were changed. The loaded helix section was designed to be in synchronism with the slow space-charge wave at all frequencies. The dispersion of the unloaded helix section was adjusted so that normal growing wave gain occurred for frequencies at the low end of the band. At the high end of the band, the phase velocity of the wave was far from synchronism so that only Crestatron interaction occurred. The purpose of this adjustment was to enhance the tube's performance at the low end of the band.

A prototype TWT was built based on this design theory. The tube achieved a bandwidth of 2.74 octaves. Large signal calculations computed the electronic efficiency to ranges between 7 and 15 percent. Figure 4b illustrates the saturation output power as a function of frequency.

Enhanced harmonic growth and degraded fundamental performance at the lower band edge clearly limits the operating bandwidth of the TWT. Viewing these results, the critical question becomes "Can a 2 to 18 GHz bandwidth be realized by a helix type TWT amplifer and still be able to obtain a reasonable efficiency across the entire frequency band?" The answer to this question is "yes." The remainder of this report describes the theoretical analysis used to investigate this question and present the conditions necessary to achieve the desired results.

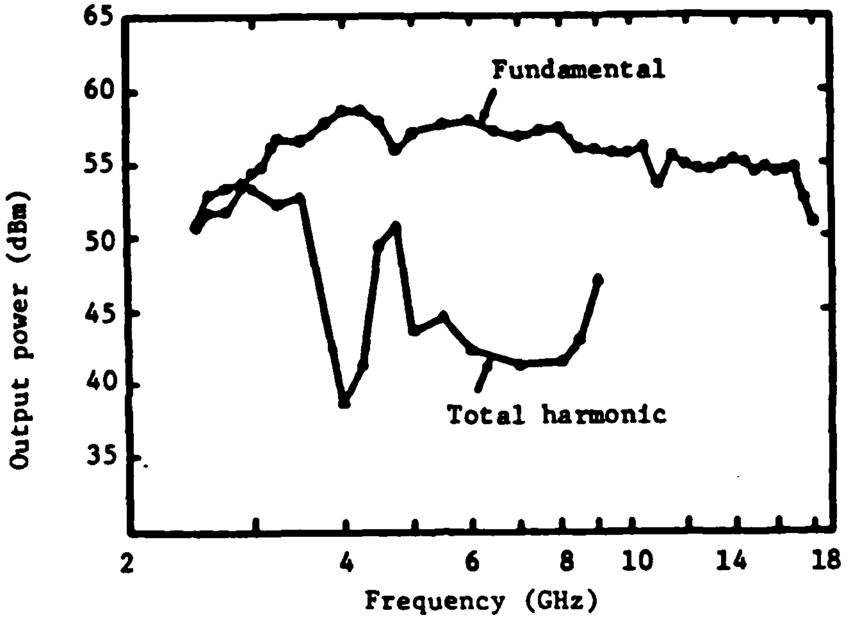

Fig. 4a. Saturated output power versus frequency for various 2.58 octave TWT described on page 8.

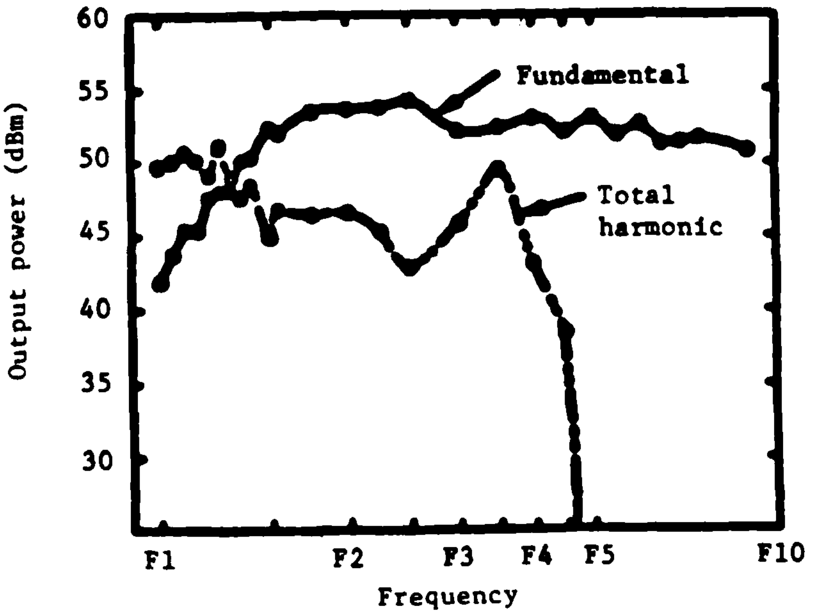

Fig. 4b. Saturated output power versus frequency for various 2.74 octave TWT described on page 11.

III. THEORETICAL DESIGN APPROACH

The main hindering factor in achieving the 3.2 octave bandwidth (2-18 GHz) has been an enhanced harmonic and a degraded fundamental power content at the lower frequency band edge. Studies[10,11] have shown that harmonic injection can be used to suppress harmonic growth and enhance fundamental performance. The problem with this approach is that external hardware, capable of generating a harmonic signal of considerable strength as well as phase shifting the signal, must be implemented. Dionne[12] and Sangster[13] have shown that by correctly shaping the dispersion of a helix RF circuit, harmonic suppression internal to the TWT can be achieved over an octave band or greater. Dionne illustrated the effects of varying the second harmonic/fundamental phase velocity and beam coupling impedance ratios. His analysis indicates that if the phase velocity ratio is chosen correctly, growth of the second harmonic will be suppressed and the fundamental efficiency will be increased. It was also shown that as the beam-coupling impedance ratio increases, harmonic power content increases, and fundamental efficiency decreases. Sangster illustrated that the harmonic power is invariant for low to intermediate values of gain parameter C.

In order to achieve the 3.2 octave bandwidth, the harmonic suppression phenomenon reported by Dionne and Sangster is analyzed and applied to the two-section output circuit concept. Several design parameters are varied in order to determine the conditions which yield optimal TWT performance. The numerical results of a computer program, which simulates the performance of a helix traveling-wave tube, are used as the basis for this study. The following parameter list defines the constants and variables used as input data to the one-dimensional large signal program.

Constant parameters:

1. Frequency band = 2-18 GHz
2. Circuit model (see Fig. 5)
    a. The input circuit electrical characteristics were chosen so that small signal interaction would occur for all frequencies in the 2-18 GHz band.
    b. The velocity characteristics of Section 2 are constant for all cases (see Fig. 6a).
    c. The impedance (as a function of circuit geometries) of the input circuit and Section 2 of the output circuit was determined from empirical data.[6]
3. Barrel (shield) diameter/helix diameter ratio = 2.34
4. Space-charge (tunnel) diameter/helix diameter ratio = 1.65
5. Electron beam diameter/helix diameter ratio = 0.328
6. Dc beam current = 255 mA
7. Number of charge groups = 37
8. Two-signal analysis (fundamental and second harmonic) for 2-9 GHz
    a. Second harmonic initial magnitude = 0.0 watts
    b. Second harmonic initial phase = 0.0 degrees
9. Single signal analysis (fundamental) for f = 10-18 GHz

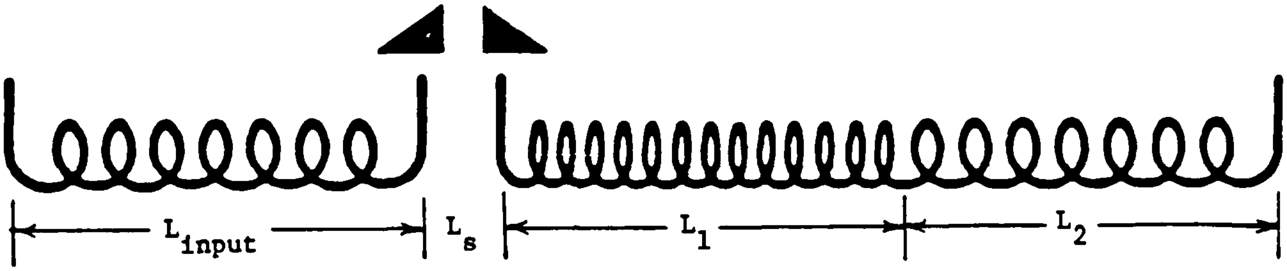

$L_{input} = 4.5$ in, $L_s = 1$ in, $L_t = L1 + L2 = 7.5$ in

Fig. 5. Schematic view of TWT circuit model.

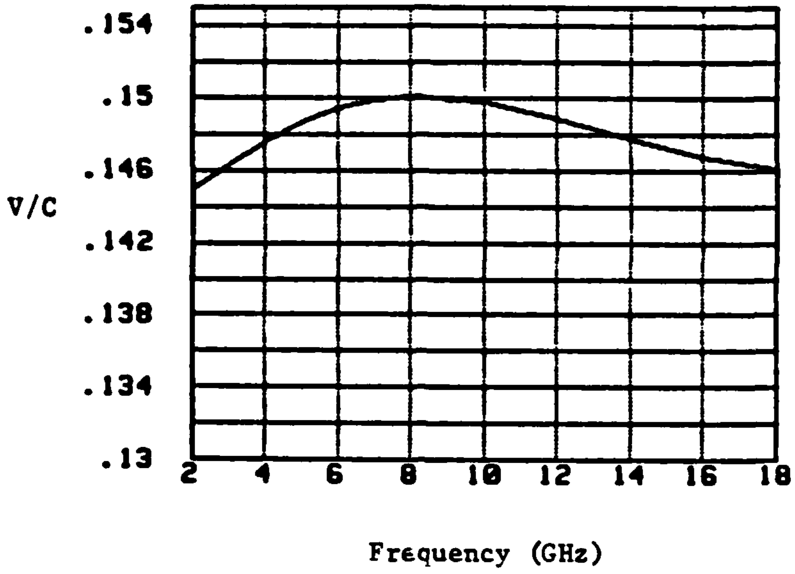

Fig. 6a. Phase velocity profile for Section 2.

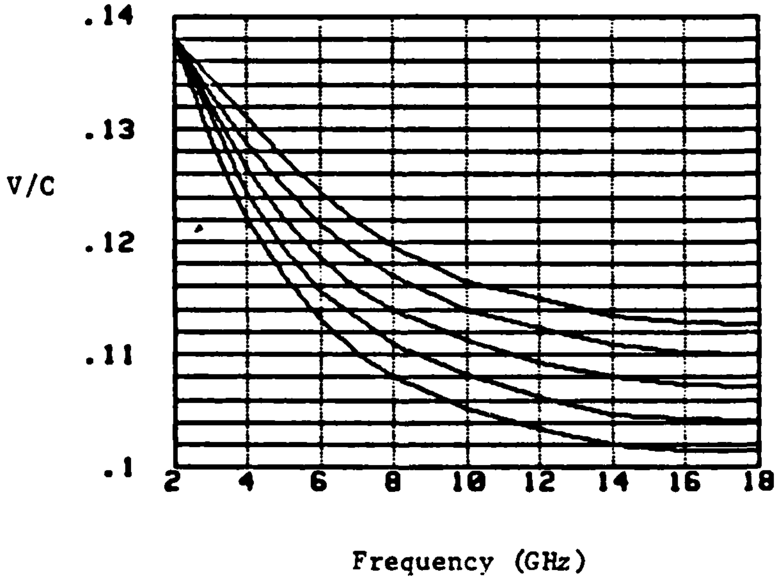

Fig. 6b. Phase velocity profile for Section 1.

Variable parameters:

10. Dispersion of Section 1 (see Fig. 6b)

11. Dc beam voltage (6.2, 6.5, 6.8, 7.1, 7.4 kV)

12. Length ratio (L_1/L_t) = 0.43 to 0.79 (see Fig. 5)

13. Impedance of Section 1 varies as a function of dispersion

The dispersiveness of Section 1 was incrementally varied in order to determine a phase relationship between the fundamental and second harmonic that resulted in a suppressed harmonic. The curves shown in Fig. 6b represent the dispersion of Section 1. Each curve has been arbitrarily shaped and is used as an individual case that is input to the large signal program. These dispersion curves are based on the premise that each can be physically realized by a helix circuit. The interaction impedance associated with these curves is determined from a relationship that defines the impedance as a function of the circuit wave phase velocity, independent of circuit geometries and loading. This enables the dispersion to be arbitrarily shaped (within limits to be discussed later).

The impedance-velocity relationship was derived using Figs. 7a and 7b, which were acquired from Putz et al.[6] on phase velocity dispersion control and are based on measured data. This report presents the experimental results of applying various types of metal loading segments to shape the dispersion characteristics of a helix RF circuit. Figure 7a displays the normalized axial impedance as a function of γa for numerous loaded helix circuits. The numbered curves illustrate the impedance

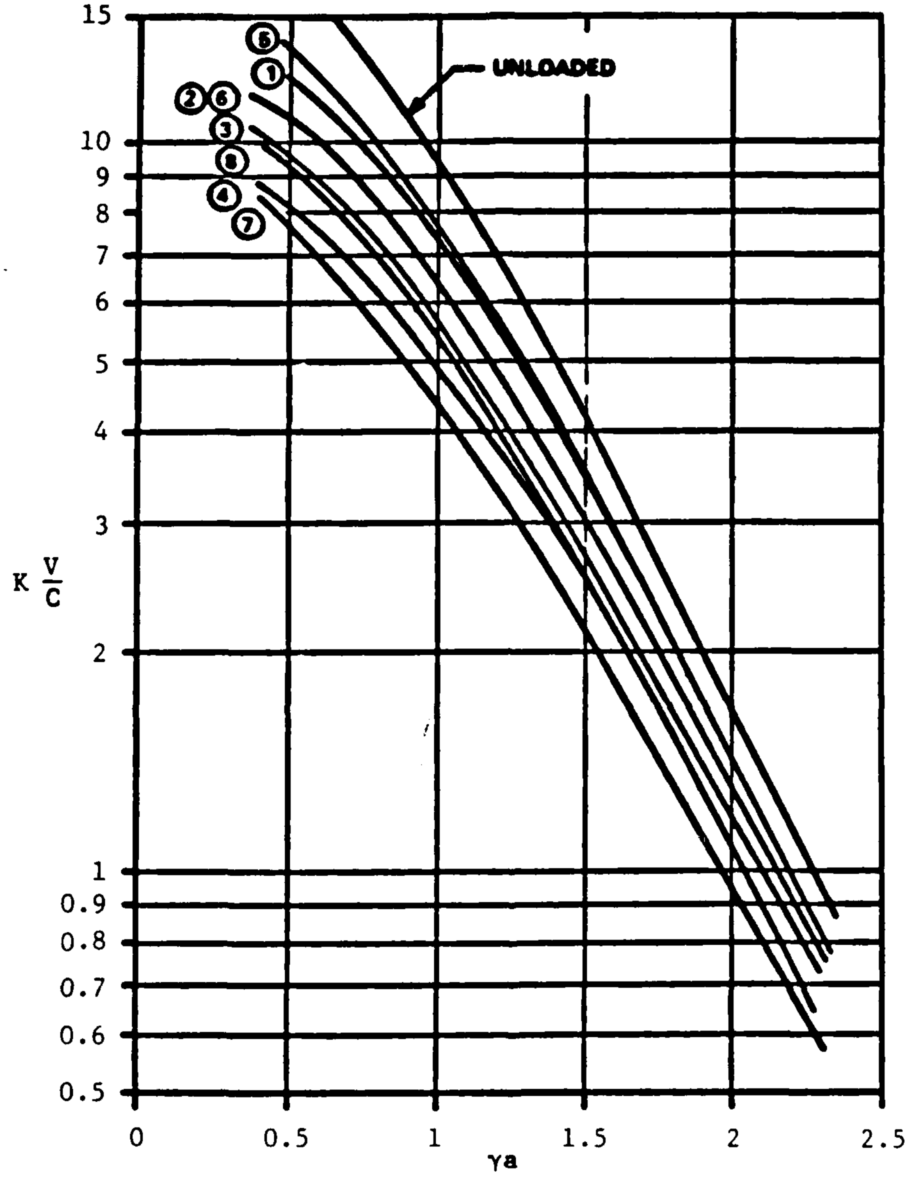

Fig. 7a. Normalized axial impedance versus γa.

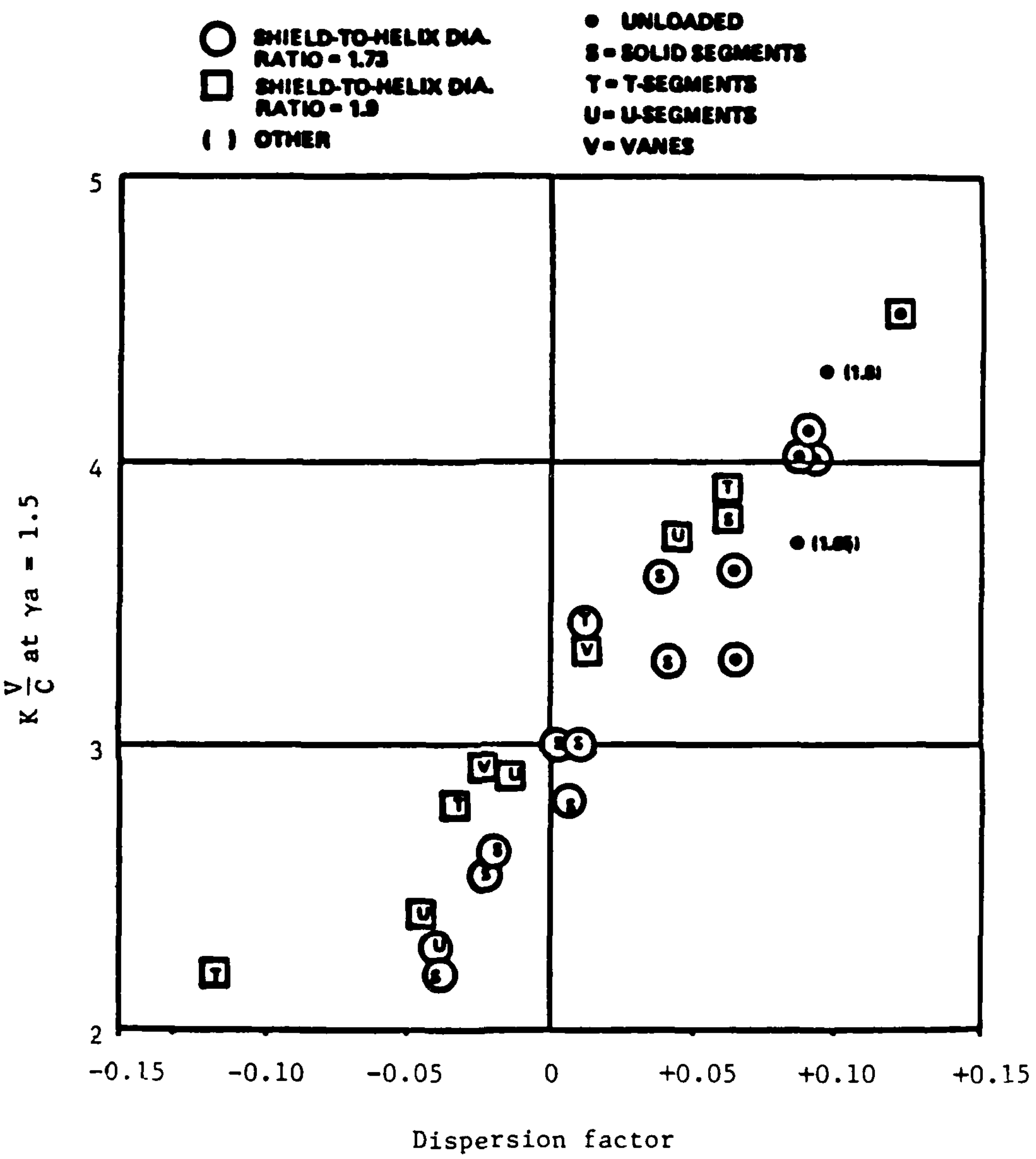

Fig. 7b. Normalized axial impedance at γa = 1.5 versus the dispersion factor.

variation due to changes in segment loading geometry. The curve labeled "unloaded" represents the impedance variation for an unloaded helix circuit. Since Section 1 is highly dispersive, this is the only curve in the figure that is used in deriving the impedance-velocity relation. Figure 7b depicts the relationship between normalized impedance and dispersion for various loading segment types and shield to helix diameter ratios. The dispersion factor (D_f) is defined as the phase velocity that occurs at $\gamma a = 0.5$ divided by the phase velocity at $\gamma a = 2$, where γa is the radial propagation constant multiplied by the helix average radius. This value is subtracted by 1 in order to present the dispersion factor as a percentage. In mathematical form, the dispersion factor is expressed as

$$D_f = \frac{v_p \text{ at } \gamma a = 0.5}{v_p \text{ at } \gamma a = 2} - 1$$

This number represents the dispersiveness of a helix circuit. A large, positive dispersion factor signifies an extremely dispersive circuit, whereas a large negative dispersion factor indicates significant negative dispersion. A D_f equal to zero represents a circuit that displays a flat, nonvarying velocity characteristic. This analysis is concerned with that region of the figure which signifies positive dispersion ($D_f > 0$).

The impedance of an unloaded helix circuit can be determined to within ±10 percent, using Figs. 7a and 7b, as long as the following criteria are satisfied:[6]

i. 1.65 < shield to helix diameter ratio < 1.9

ii. $0 < D_f < 0.15$

iii. $0.25 < \gamma a < 2.5$

Given the phase velocity versus frequency characteristics of a helix circuit, the dispersion factor can be easily calculated using the above equation. Once D_f is known, the normalized impedance (K v/c) at γa = 1.5 can be graphically determined from Fig. 7b. This value is then plotted on Fig. 7a, and the "unloaded" impedance curve is superimposed onto this point. The assumption is that the impedance will scale. This is confirmed by the measured circuits (numbered curves) illustrated in the figure. The normalized impedance of this circuit for any γa (or frequency) can be calculated using this new curve. This graphical method was developed into a computer program which uses the dispersion as input and calculates the impedance at selected frequencies (within the limits of criteria iii as output).

In order to predict the impedance as a function of dispersion with minimum error, mathematical expressions had to be derived which accurately approximated the curve in Fig. 7a, and "fit" the data points in Fig. 7b. A cubic spline routine was used as the mathematical representation for the curve in Fig. 7a. Most cubic spline routines display erratic behavior at the end points because the first and second derivatives are set to zero. This routine was found to accurately interpolate data near the end points. The reason for this was due to a three point difference method used at the end points to approximate the first and second derivatives. The data points illustrated in Fig. 7b indicate a linear variation over the limits specified by criterion ii. It must be determined whether this variation remains linear beyond Df = 0.15 because the dispersion curves for Section 1 (Fig. 6b) have a D_f ranging between 0.14 and 0.21. Appendix A details this analysis. It was concluded that a linear approximation would be used to fit the data points of Fig. 7b.

The shield-to-helix diameter ratio, stipulated by criterion 3, exceeds the limit specified by criterion i. A comparison between the calculated and measured impedances of a helix circuit with this geometrical ratio and Df equal to 0.15 indicated a maximum impedance deviation of -3 percent over the lower half of the frequency band.

IV. LARGE SIGNAL THEORY

A. Assumptions

The nonlinear behavior of a traveling-wave tube amplifier can be calculated by numerically integrating the motion of the electrons in the presence of the circuit and space-charge fields. The large signal theory used in the computer program is based on a version of the Tien[15] approach, which has been modified by Kino.[16] The theory that is used to express the electric field due to the space charge was derived by Wallander.[17] The circuit equations, the equation of motion, and the equation of conservation of charge are the basic equations from which the theory is derived.

The assumptions made in this analysis are:

1. The derivation is based on a one-dimensional approach. The transverse motions of the electrons are neglected, and the current, velocity, and fields are functions of axial distance and time.
2. The fundamental and second harmonic components of the current excite waves on the circuit.
3. The electrons are modeled by uniformly charged disks of finite volume. The disks are concentric with the helix and have a radius equal to the beam radius.
4. Interaction between the RF wave and the electron beam occurs in the zeroth and -1 space harmonic components of the total circuit field at each frequency.

5. Magnetic field effects are omitted.

6. The circuit is lossless.

B. Circuit Equations

The large signal theory is based on modeling the helix RF circuit as a transmission line with coupling to the beam. The circuit equations[18] are

$$\frac{\partial V}{\partial x} = -L\,\frac{\partial I}{\partial t} - RI$$

$$\frac{\partial I}{\partial x} = -C\,\frac{\partial V}{\partial t} - GV - K\,\frac{\partial \rho_\omega}{\partial t}$$

where

$\frac{\partial V}{\partial t}$	is the time rate of change of the voltage
$\frac{\partial I}{\partial t}$	is the time rate of change of the current
L	is the inductance per unit length
C	is the capacitance per unit length
R	is the resistance drop per unit length
G	is the conductance across the line per unit length
$\frac{\partial \rho_\omega}{\partial t}$	is the beam coupling term
K	is a constant multiplying factor

The characteristic impedance (Z_o) and the circuit wave phase velocity (v_o) are defined as

$$Z_o = \sqrt{L/C}$$

$$v_o = \frac{1}{\sqrt{LC}}$$

The circuit equations in terms of the impedance and velocity are

$$\frac{\partial V}{\partial x} = - \frac{Z_o}{v_o} \frac{\partial I}{\partial t} - RI$$

$$\frac{\partial I}{\partial z} = - \frac{1}{Z_o v_o} \frac{\partial V}{\partial t} - GV - K \frac{\partial \rho_\omega}{\partial t}$$

Tien expresses the behavior of a transmission line in terms of traveling waves rather than voltage and current. Following this approach, the forward wave (F) and the backward wave (B) are defined as

$$F = \frac{V + IZ_o}{Z}$$

$$B = \frac{V - IZ_o}{Z}$$

The circuit equations become

$$\frac{\partial}{\partial z} \left(F + B\right) = - \frac{1}{v_o} \frac{\partial}{\partial t} \left(F - B\right) - \frac{R}{Z_o} \left(F - B\right) \qquad (1.a)$$

$$\frac{\partial}{\partial z}\left(F - B\right) = -\frac{1}{v_o}\frac{\partial}{\partial t}\left(F + B\right) - GZ_o\left(F + B\right) + \left(F - B\right)\frac{\partial}{\partial z}\left(\ln Z_o\right) - K\frac{\partial \rho_\omega}{\partial t} \tag{1.b}$$

and the forward and backward circuit waves are assumed to be of the form

$$F(t,z) = \frac{Z_oI_o}{4}\left\{a_1(y)\cos m\phi - a_2(y)\sin m\phi\right\}$$

$$B(t,z) = \frac{Z_oI_o}{4}\left\{b_1(y)\cos m\phi - b_2(y)\sin m\phi\right\}$$

where

y is the normalized axial distance

ϕ is the phase $\omega t - \beta_e z$

m is the harmonic number ($m = 1, 2, 3, \ldots$)

I_o is the beam current

a_1, a_2, b_1, b_2 are the forward- and backward-wave component amplitudes

C. Equations of the Beam

The equation of motion is expressed as

$$\frac{d^2z}{dt^2} = -\eta E$$

where $\eta = \frac{|e|}{m}$, and the term $\bar{v} \times \bar{B}$ is neglected. The total electric field is defined as

$$E = E_{circuit} + E_{sc}$$

where the circuit field is calculated by differentiating F and B with respect to z. The space-charge field is determined by using the Wallander space-charge theory, which is based on a Fourier analysis of the RF current in the beam.

The Wallander analysis begins with Maxwell's equation,

$$\bar{\nabla} \times \bar{H} = \bar{i} + \frac{\partial \bar{D}}{\partial t} = 0$$

From this equation, a relation for the amplitude (Em) of the mω component of Esc is expressed as

$$j m \omega \varepsilon_o E_m + R_m^2 i_m = 0$$

which yields

$$E_m = - \frac{R_m^2 i_m}{j m \omega \varepsilon_o} \tag{2}$$

Olving and Wallander,[19] in their analytical treatment of the solid disk beam, derive the reduction factor R_m to be

$$R_m = \left[1 - 2 I_1(m\beta_e b) K_1(m\beta_e b) - 2 \frac{K_o(m\beta_e a)}{I_o(m\beta_e a)} I_1(m\beta_e b) \right]^{1/2}$$

where

a = space-charge tunnel (conducting boundary) radius

b = beam radius

$I_o(\arg)$, $I_1(\arg)$, $K_o(\arg)$, $K_1(\arg)$ = modified Bessel functions

The RF beam current density is expanded in a Fourier series,

$$\frac{\partial \rho_\omega}{\partial t} = i(t,z) = \sum_{m=1}^{m} i_m(z)\, e^{jm\phi}$$

where i_m is the Fourier amplitude of the $m\omega$ component. Similarly, the axial space-charge field is written as

$$E_{sc}(t,z) = \sum_{m=1}^{m} E_m(z)\, e^{jm\phi} \tag{3}$$

The amplitudes of the Fourier components of the current density are expressed as

$$i_m = \frac{1}{2\pi} \int_{-\pi}^{\pi} i\, e^{-jm\phi}\, d\phi$$

By conservation of charge, the above equation becomes

$$i_m = \frac{i_o}{2\pi} \int_{-\pi}^{\pi} e^{-jm\phi(\phi_o)}\, d\phi_o \tag{4}$$

where $\phi(\phi_o)$ is the phase position ϕ of a disk that has an initial phase position ϕ_o.

In performing the computer calculations, N is equal to the total number of disks, and n is an integer with limits $0 < n < N$. It is assumed that ϕ varies linearly with ϕ_o between disks n and n + 1. Then Eq. 4 can be written as

$$i_m = \frac{i_o}{2\pi} \sum_{n=0}^{N-1} \int_{-\pi}^{\pi} e^{-jm\phi(\phi_o)} \, d\phi_o \qquad (5)$$

where

$$\phi(\phi_o) = \phi_n + \frac{\phi_{n+1} - \phi_n}{\phi_{o_{n+1}} - \phi_{o_n}} (\phi_o - \phi_{o_n}) \; , \; \phi_{o_n} < \phi_o < \phi_{o_{n+1}}$$

Equation 5 gives the current density amplitude with respect to all the disks at a distance z for each harmonic component. Introduction of Eq. 5 into Eq. 2, and substituting this expression into Eq. 3 gives the space-charge field working upon disk n at a distance z from the input

$$E_{sc}(n,z) = - \sum_{m=1}^{M} \frac{R_m^2}{jm\omega\varepsilon_o} \cdot i_m(z) \, e^{jm\phi_n} \qquad (6)$$

The large signal program developed at Varian Associates is based on the above equations, but incorporates proprietary modifications. The set of equations comprising the circuit and beam equations are solved separately for each harmonic component. The kinetic energy lost by the beam is calculated for each harmonic component specified. This information is used to determine the total energy balance, which indicates the accuracy of the large signal computation. The energy balance gives the difference between the kinetic energy lost by the beam and the sum of the energies given up to the load and lost on the circuit and in the sever, and is expressed as a percentage of the initial beam energy. A study performed by Putz,[20] which compared large signal calculations against TWT measurements, reported that the best correlations occurred for energy balances in the range ±1 percent. The energy balances of the large signal calculations presented in the next chapter had a mean value of 0.14 percent, and a 0.603 standard deviation.

D. Computer Program Input Parameters

The computer program calls for numerous input data. Many of these parameters are crucial to accurately predicting a TWT's performance. Two important parameters are the number of electron disks (N) used in the calculation and the integration step size (Dy). In order to determine a value for the number of disks, the percent change in fundamental output power as a function of N was computed. The value N = 37 was found to give a reasonable compromise between cost, running time, and accuracy. A similar exercise could be performed with respect to the integration step size. Instead, the default value Dy = 0.01 was used. Another important parameter is the tunnel diameter. This diameter is used as the boundary for the space-charge field. It has been argued[21] that a helix surrounded by a barrel will appear transparent to the space-charge fields, thus the barrel should be used as the tunnel diameter. Putz has shown that neither the helix nor the barrel diameter is consistently best. The average between the helix and barrel diameters was used as the approximate value for the tunnel diameter.

Other crucial input parameters are the circuit velocity and impedance, loss, and beam diameter. In many cases, the circuit velocity can be obtained from automatic network analyzer (ANA) measurements. For this study, the velocities and impedances are based on the analysis presented in Chapter 3. The cold circuit loss can be measured by the

ANA, but is unknown under TWT operating conditions. The circuit loss input to the program was assumed to be zero at all frequencies. The reason for this assumption was to reduce the amount of program input. The diameter of the electron beam is usually estimated from the magnetic focusing field value or measurements made on a beam analyzer. Beam diameter changes at numerous axial positions can be input in order to model beam expansion. The beam diameter input to the program was left as a constant value over the length of the tube for all calculations made in this study.

For traveling-wave tubes that are designed for multioctave operation, multiple harmonics should be used when simulating the tube's performance at the low end of the band. The analysis presented by this paper uses the second harmonic in the calculation for fundamental frequencies 2 through 9 GHz, and only the fundamental component for frequencies 10 through 18 GHz. Multiple harmonics were not used, since they would be far from synchronism. The second harmonic is the most dominant. Also, incorporating more harmonics in the analysis would greatly increase the amount of input combinations and complicate the study of the fundamental and harmonic phase effects.

The above discussion mentioned some of the important input parameters and considerations for minimizing the deviation between large signal predictions and actual TWT measurements, and pointed out the assumptions and input conditions used in this study. It can be concluded that the effect of these assumptions will produce some error in the efficiency calculation. Using previous multioctave circuit designs as input and applying the assumptions stated above, the large signal calculations predicted the power output at saturation to be as much as 4 dBm higher than measured values at the low frequency end of the band, and as much as 3 dBm at the high end. The numerical results, though, did accurately predict the frequency where the harmonic became dominant over the fundamental.

The data presented in the next chapter were obtained by running the large signal code on a 3081-type IBM computer. The phase-trajectory plots and the normalized current amplitude phase plots were created by a 9816-type Hewlett Packard computer.

V. ULTRA-BROADBAND THEORY BASED ON TWT COMPUTER SIMULATION

A. Definitions

The emphasis of this analysis is placed upon the dependencies of the injection velocity parameters (b1 and b2), the phase velocity ratio (Vh/Vf) on second harmonic suppression (Ph/Pf), and the saturation efficiency at f = 2 GHz, where

b1 = injection velocity of Section 1 (fundamental component)
b2 = injection velocity of Section 2 (fundamental component)
C1 = gain parameter of Section 1 (fundamental component)
C2 = gain parameter of Section 2 (fundamental component)
Vh = second harmonic circuit wave phase velocity on Section 1
Vf = fundamental circuit wave phase velocity on Section 1
Pf = fundamental output power content
Ph = second harmonic output power content

The effect of varying the length of Section 1 and utilizing Crestatron efficiency is also discussed.

The following plots presented in this chapter are based on saturation data. The phase trajectory plots and normalized current amplitude plots are used to explain the interaction occurring between the fields and beam. It is recommended that the reader refer to Appendix C, which gives a brief explanation of the information obtained from these plots.

B. Harmonic Suppression and Electronic Efficiency Analysis

The effect of the phase velocity ratio of Section 1 on second harmonic suppression and saturation efficiency at the output for f = 2

GHz is displayed in Figs. 8a and 8b. Figure 8a shows that the degree of harmonic suppression is extremely dependent on Vh/Vf. The highest degree of suppression occurs for Vh/Vf = 0.90. Maximum suppression will result if the injection velocities b1 and b2 are correctly chosen. Figure 8b indicates that the highest degree of harmonic suppression is accompanied by the greatest fundamental efficiency. The kinetic energy lost by the second harmonic circuit field to the beam is gained by the fundamental.

The phase velocity ratios are based on the dispersion curves shown in Fig. 6b. The output circuit length ratio was set at $L_1/L_t = 0.55$. The effect of the circuit length on efficiency and second harmonic suppression is discussed later in this chapter.

Figures 9a through 9d display the interaction between the electron beam and the RF circuit field for the case f = 2 GHz, Vh/Vf = 0.95, b1 = 1.29, and b2 = 1.055. This case illustrates the undesirable effects of an incorrect dispersion design for Section 1. The output circuit length versus gain is shown in Fig. 9a. The gain curves show that the second harmonic circuit wave becomes dominant over the fundamental circuit wave, resulting in premature saturation of the fundamental. Figure 9b displays the electron bunching phenomenon with respect to axial position and the fundamental and second harmonic circuit field regions. The figure shows that two primary electron bunches occur at z equal to 3 to 4.5, and 4 to 6, respectively. The first bunch occurs in a decelerating fundamental and second harmonic field region, thus both circuit wave frequency components grow. The second bunch appears in an accelerating fundamental field region and a decelerating harmonic field region.

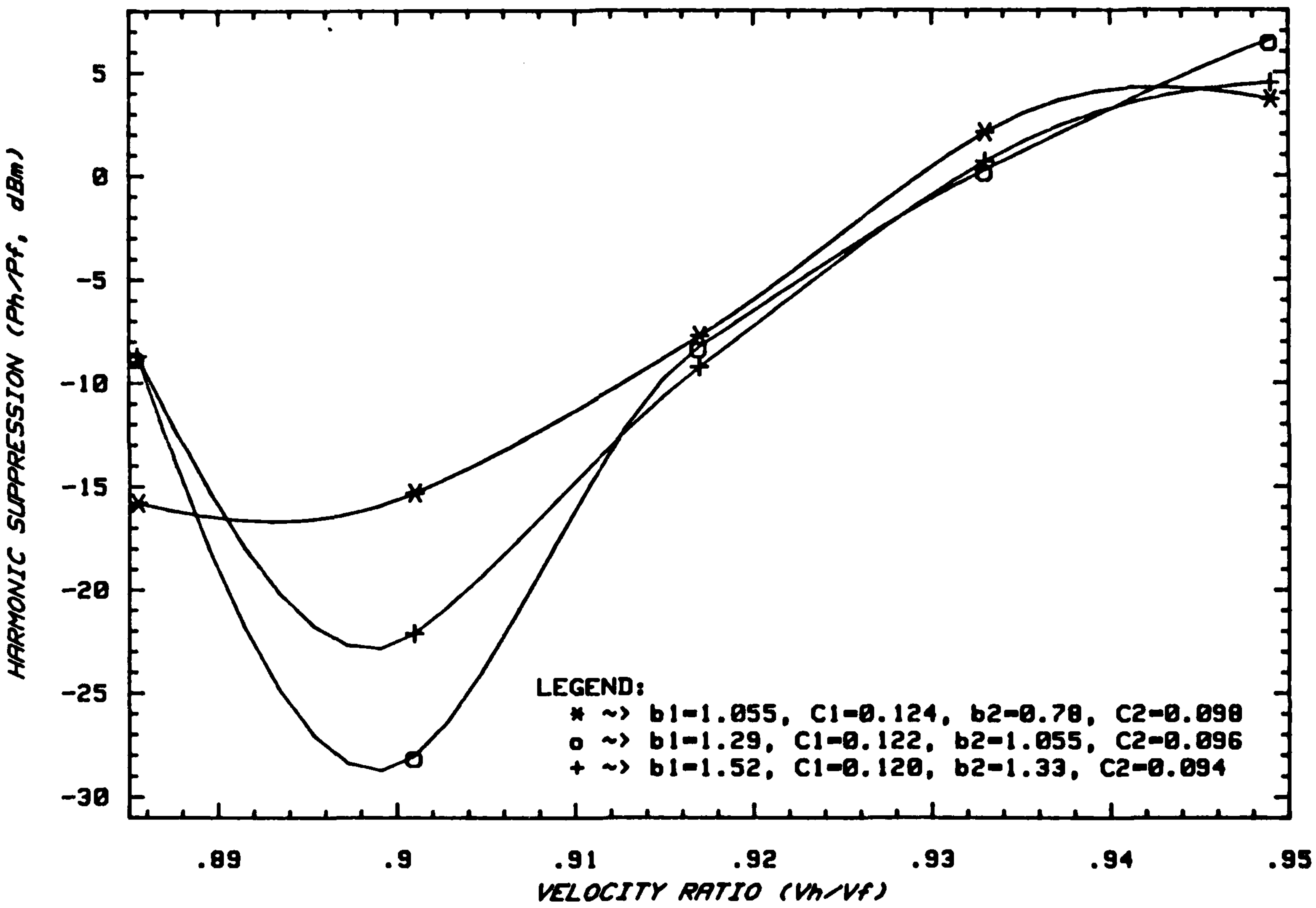

Fig. 8a. The effect of dispersion on 2nd harmonic suppression (F = 2 GHz, L1/Lt = 0.55).

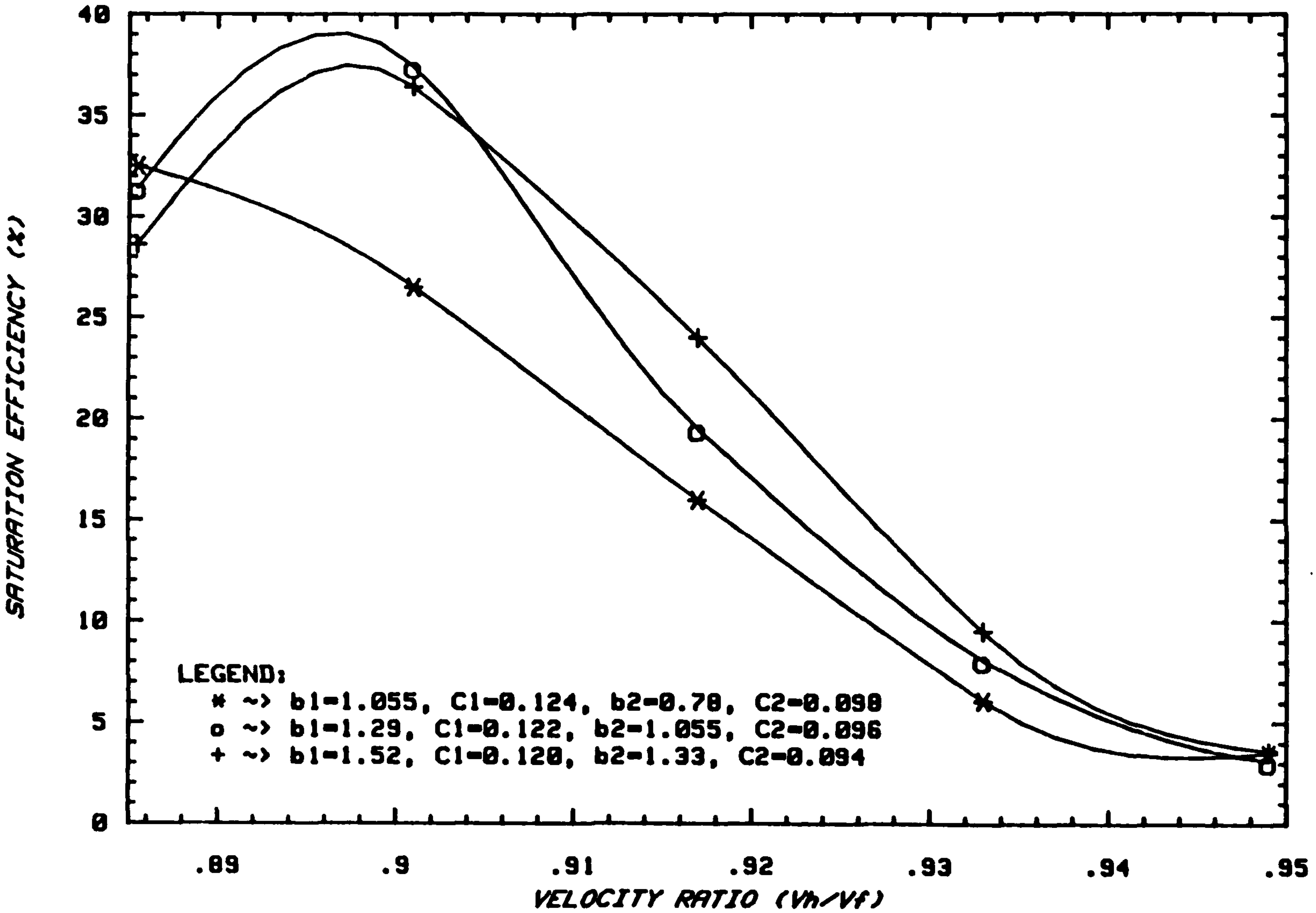

Fig. 8b. The effect of dispersion on saturation efficiency (F = 2 GHz, L1/Lt = 0.55).

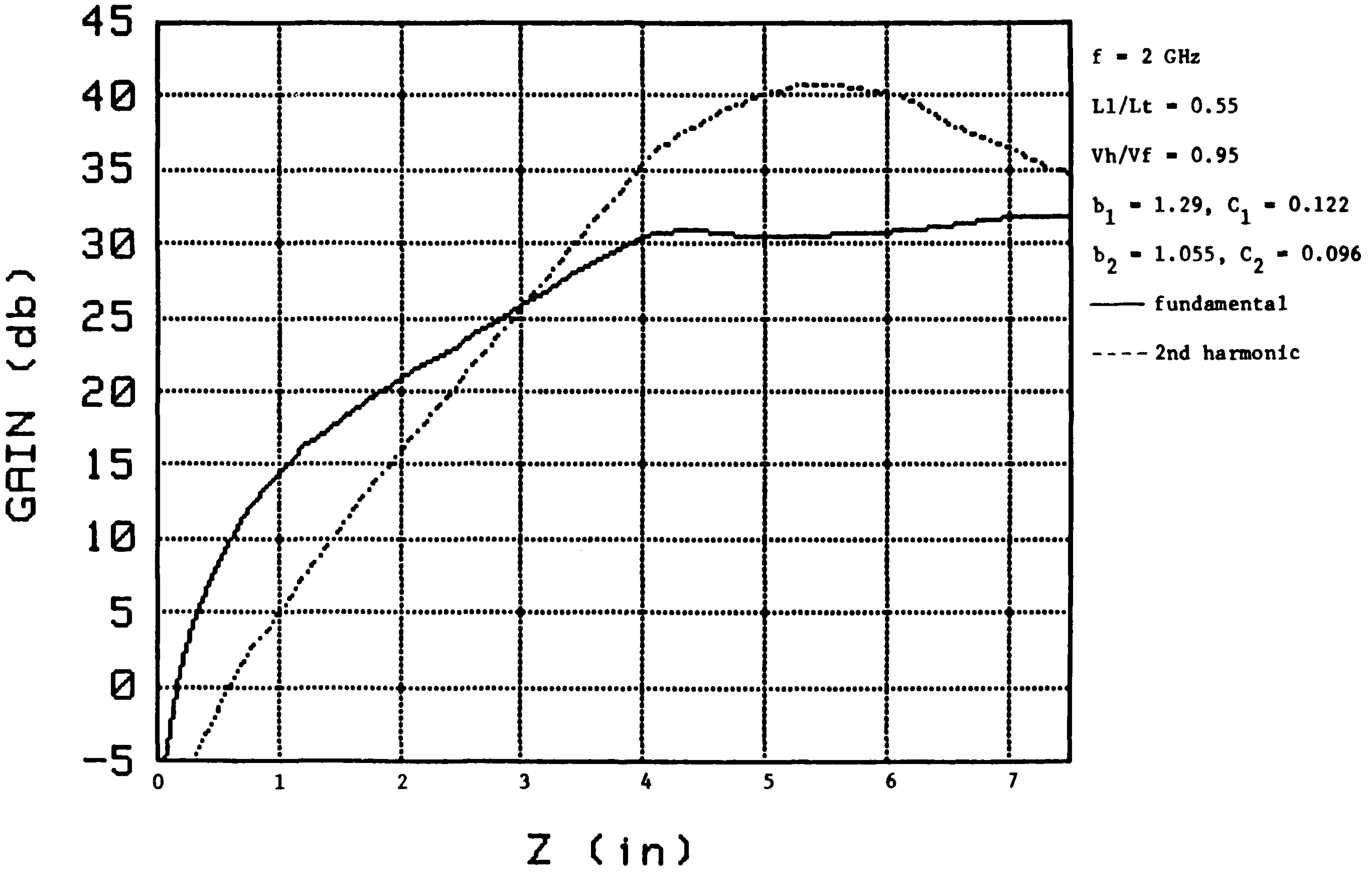

Fig. 9a. Gain versus output circuit length.

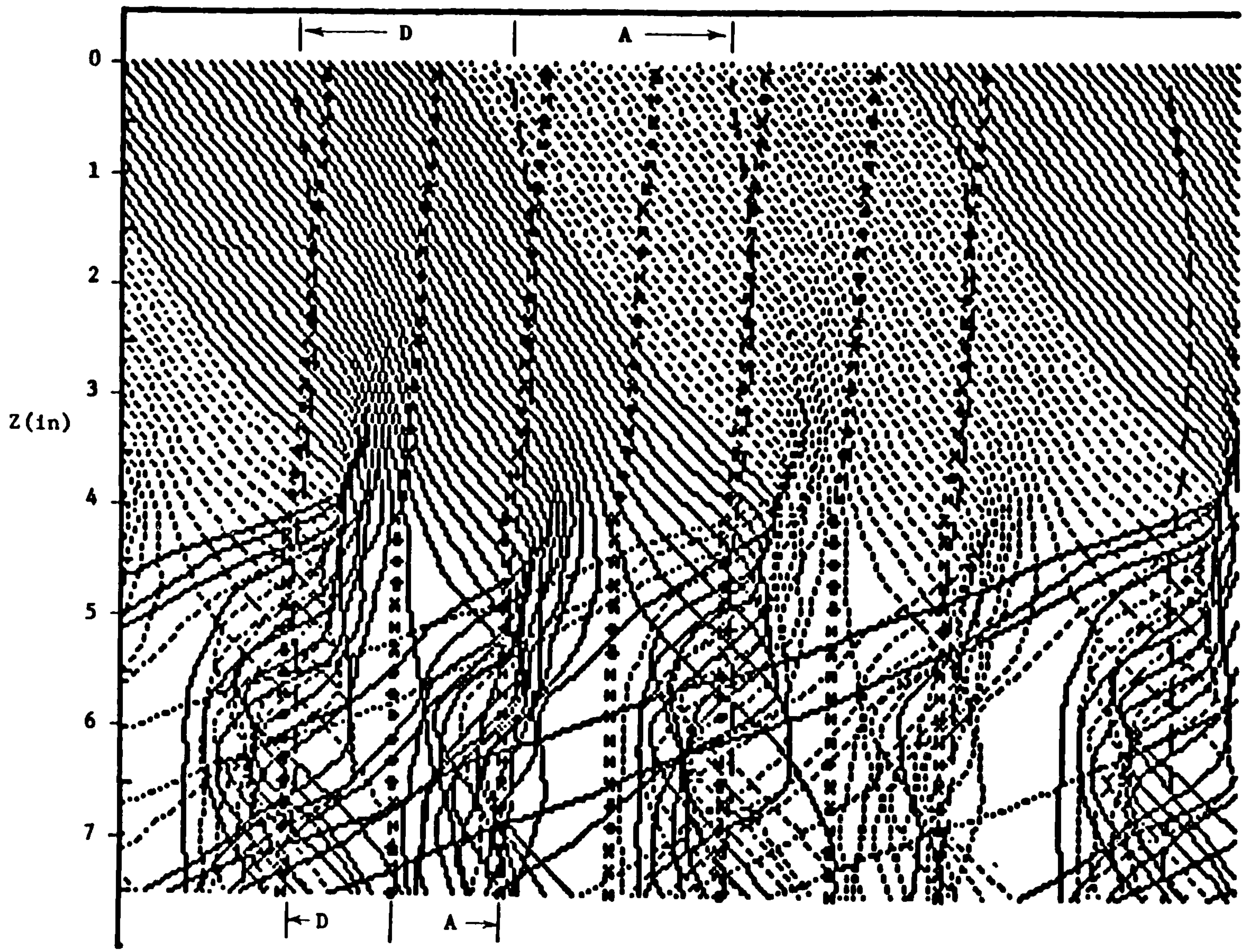

Fig. 9b. Phase trajectory versus output circuit length.

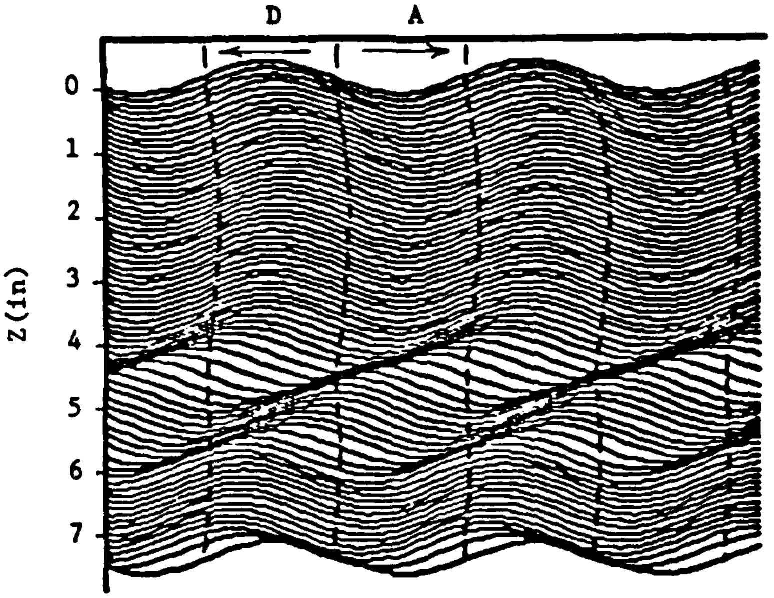

Fig. 9c. Normalized current amplitude versus output circuit length (fundamental component).

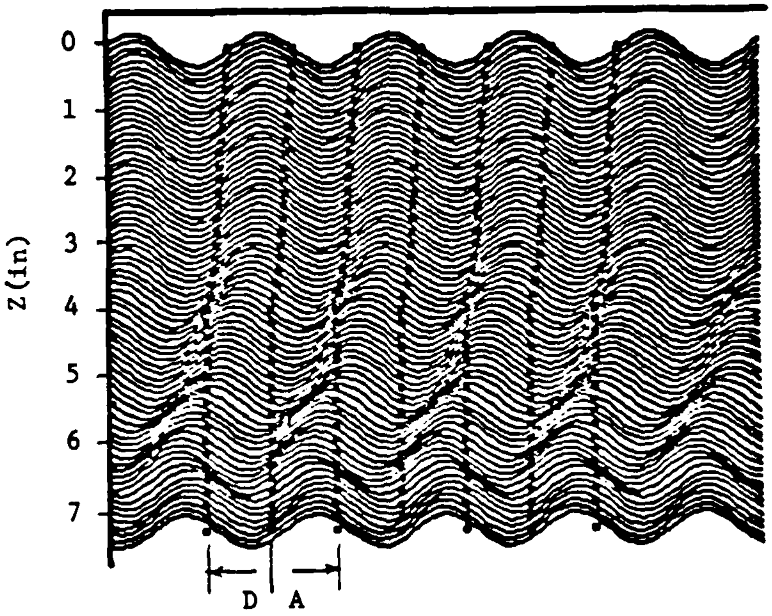

Fig. 9d. Normalized current amplitude versus output circuit length (2nd harmonic component).

The harmonic continues to grow usurping the kinetic energy given up to the beam by the fundamental forcing the fundamental circuit wave component into premature saturation. At approximately $z = 6$, the harmonic circuit field forces the decaying bunch back into an accelerating harmonic field region, and the second harmonic saturates.

Figures 9c and 9d display this phenomenon from a different perspective. The fundamental and second harmonic current amplitudes displayed in these figures correspond to the location of the electron bunches within the circuit field regions. In Fig. 9c, the current amplitude of the fundamental component remains within a fundamental decelerating field region over the first half of the output circuit length. At approximately $z = 4$, the current amplitude begins to slip back in phase into an accelerating field region resulting in the extraction of kinetic energy from the circuit field by the electron beam. At approximately $z = 6$, the fundamental beam current has completed a 2π radian phase shift back into a decelerating field region. The electron bunch has already begun to deteriorate so that only a fraction of the energy lost to the beam is recovered by the circuit wave.

Figure 9d displays the second harmonic current amplitude alignment with the second harmonic circuit field. The figure shows that the harmonic current stays within a decelerating harmonic field region beyond the point where the fundamental current slipped back into an accelerating field. The second harmonic circuit wave grows at the expense of the fundamental. At approximately $z = 5.5$, the primary bunch is pushed by the harmonic decelerating circuit field into an accelerating harmonic field region. The bunch deteriorates and the harmonic circuit wave component saturates.

Optimal synchronism between the RF beam current and the circuit field for fundamental growth and harmonic suppression occurs when the fundamental component of the RF current remains within the decelerating circuit field region for the entire length of the output circuit, thus maximum energy is extracted from the beam. The second harmonic frequency component of the RF current shifts into an accelerating harmonic circuit field at an axial position far in advance of the output, so that the harmonic circuit field gives up its energy to the beam. This mode of operation is displayed in Figs. 10a through 10d. These figures illustrate the interaction of the RF beam current with the circuit field for the case f = 2 GHz, Vh/Vf = 0.901, b1 = 1.29, and b2 = 1.055.

Figure 10a displays the fundamental and second harmonic gain variation over the length of the output circuit. The figure clearly shows the desired result -- enhanced fundamental growth and a suppressed second harmonic. The electron bunching with respect to the circuit field regions and axial position is shown in Fig. 10b. This figure shows that by correctly designing the dispersion of Section 1, the second harmonic RF component of the circuit field will lag in phase with respect to the fundamental, so that at the Section 1-Section 2 junction, the second harmonic circuit field has undergone a π radian phase shift (second harmonic phase units) with respect to the fundamental. The relative phase difference between the second harmonic and fundamental circuit field components remains essentially constant after the junction due to the nondispersive velocity characteristics of Section 2. Because

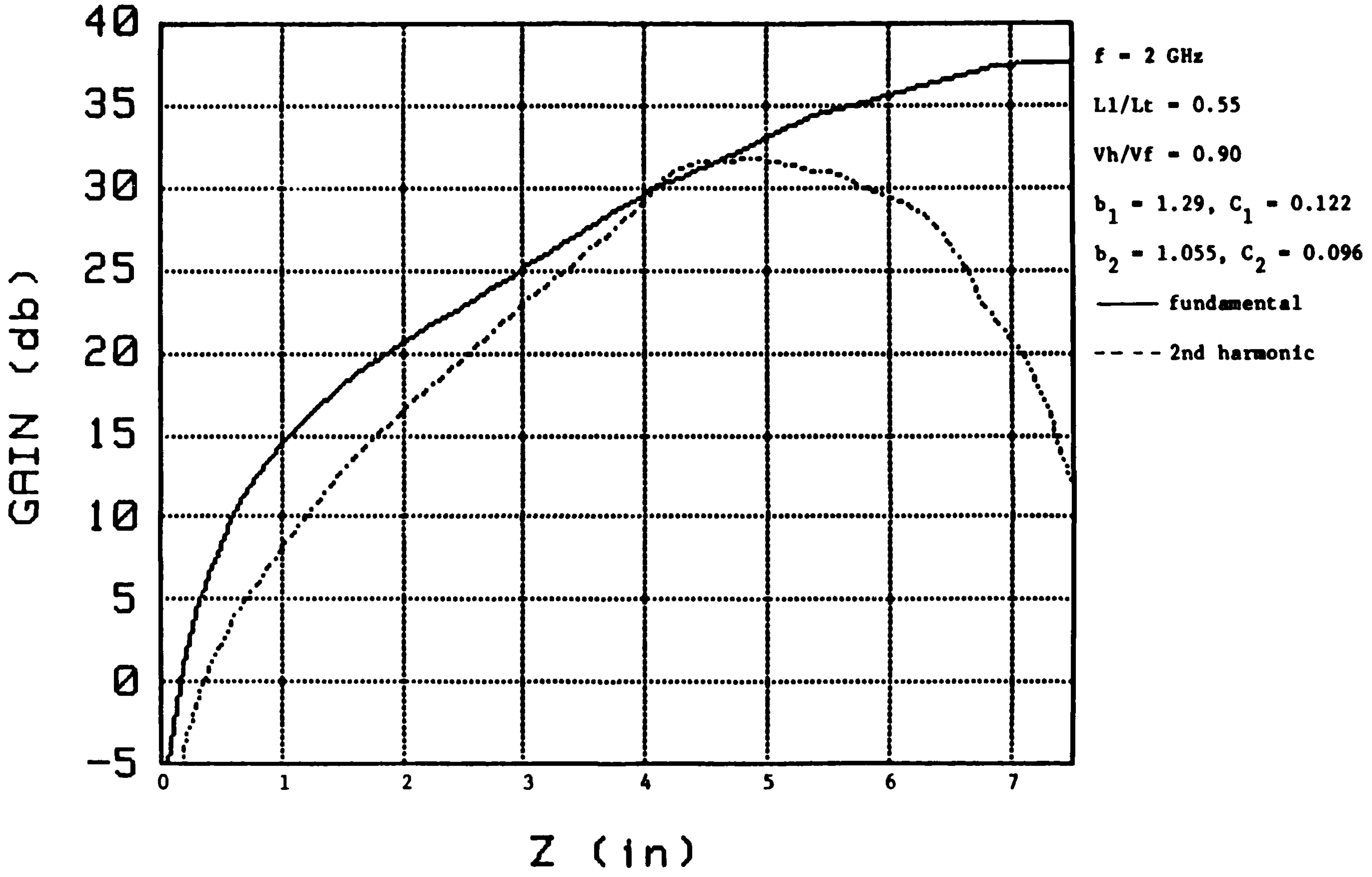

Fig. 10a. Gain versus output circuit length.

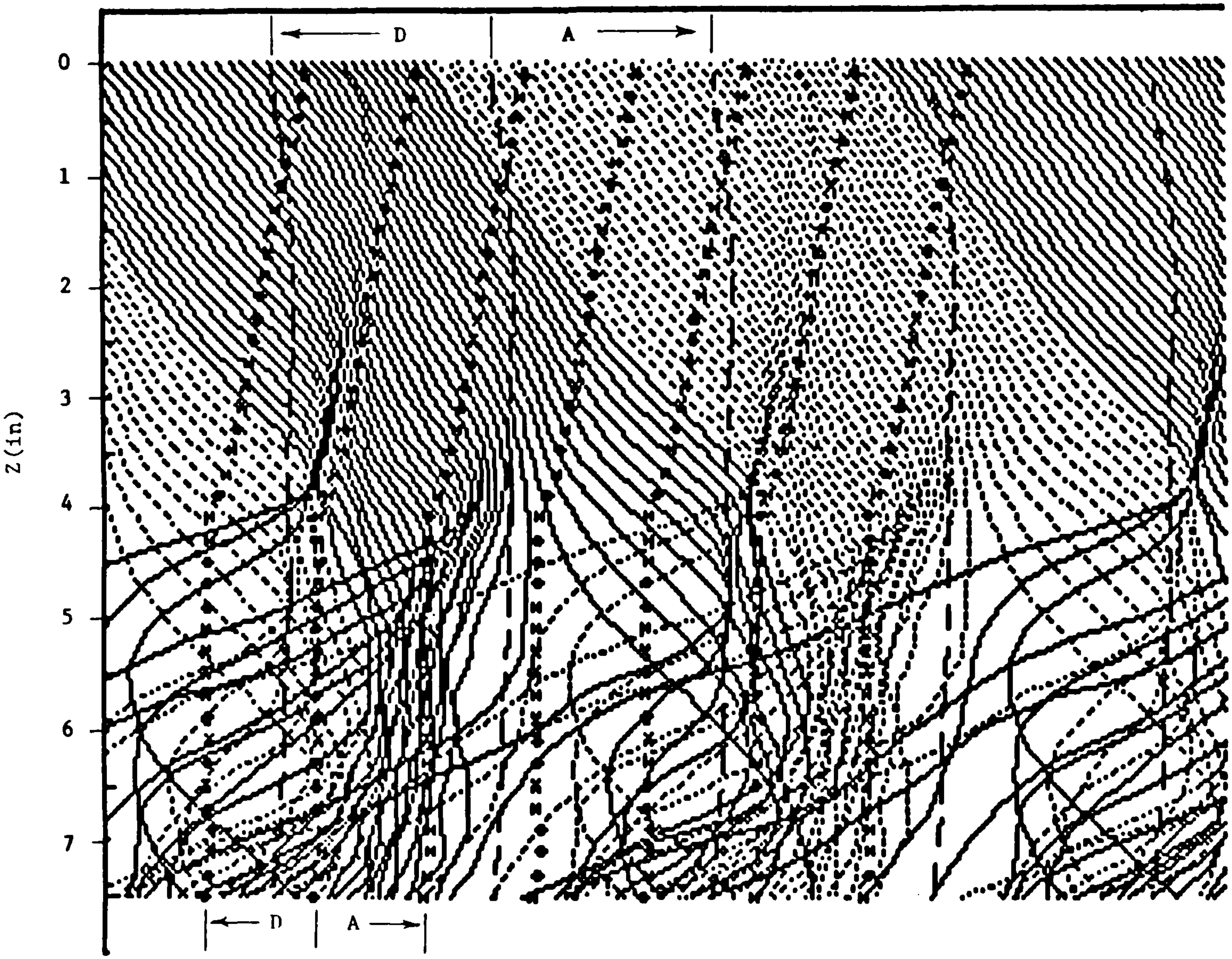

Fig. 10b. Phase trajectory versus output circuit length.

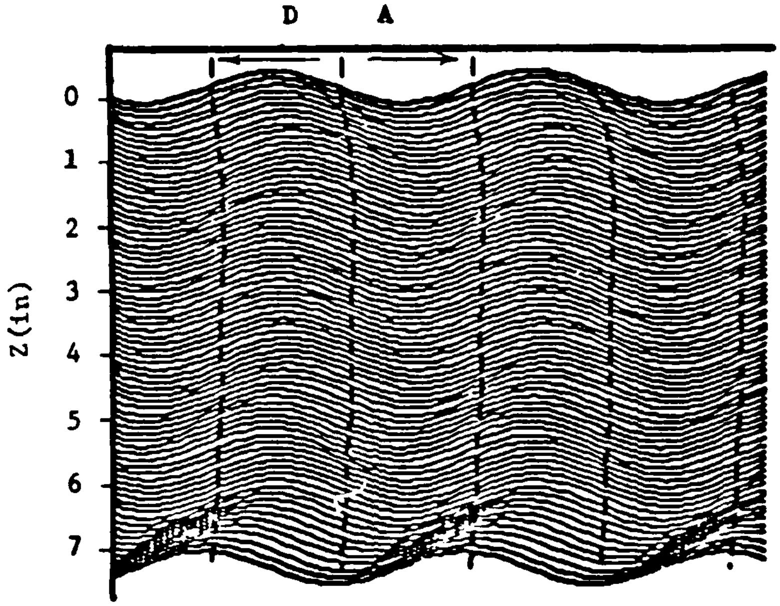

Fig. 10c. Normalized current amplitude versus output circuit length (fundamental component).

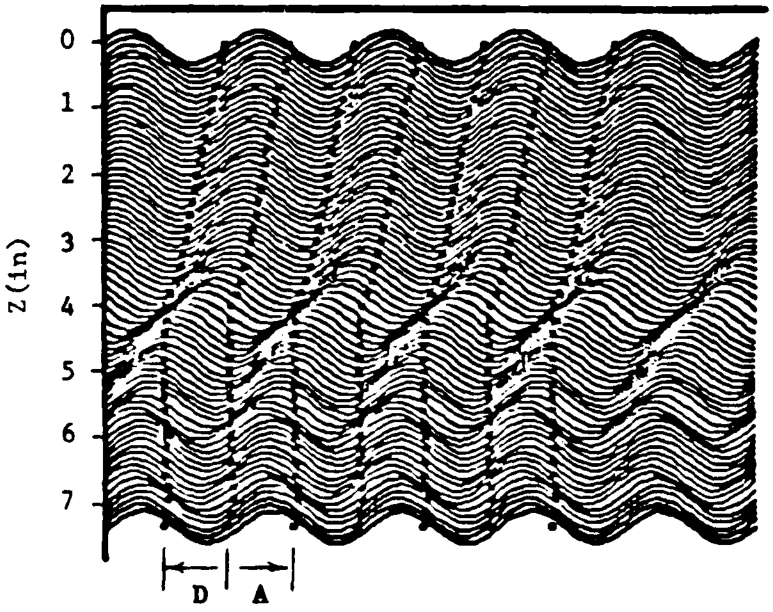

Fig. 10d. Normalized current amplitude versus output circuit length (2nd harmonic component).

of the second harmonic field phase shift, electron bunching occurs within the desired field regions. (Referring back to Fig. 9b, the harmonic field has roughly undergone a phase shift less than $\pi/2$ radians. Bunching occurs within an undesirable RF field configuration.)

The first bunch occurs between z = 2.5 and 4, and is within the decelerating fundamental and second harmonic circuit field regions, so both waves grow. A second bunch begins to form at approximately z = 3.5 in the decelerating fundamental and second harmonic field regions. At z = 4.5, the decelerating circuit field regions push the bunch back into an accelerating harmonic field region. The harmonic field gives up its energy to the beam and becomes suppressed. The combined forces of the decelerating fundamental field and the accelerating harmonic field cause the electrons to stay bunched and remain within this circuit field configuration. At the end of the output circuit, the harmonic field has become sufficiently attenuated. The decelerating fundamental field forces the electron bunch to deteriorate, and saturation occurs.

Figures 10c and 10d display the phase location of the fundamental and second harmonic beam current amplitudes within their respective circuit field regions. In Fig. 10c, the fundamental current remains within a decelerating circuit field region the length of the output circuit, thus the circuit field extracts energy from the beam and the circuit wave grows. At the output, the current amplitude begins to slip into an accelerating fundamental field region, and saturation results. This correlates with the electron bunch being forced by the decelerating circuit field into an accelerating field.

Figure 10d shows the normalized second harmonic current shifting from a decelerating harmonic field region into an accelerating field region at approximately $z = 4.5$. The second harmonic circuit field gives up its energy to the beam, and the harmonic circuit wave decays.

C. Analysis of the Crestatron Interaction Phenomenon

The basic theory of the Crestatron interaction phenomenon was described in Chapter 2. In order to determine whether this phenomenon can be utilized in the ultrabroadband circuit design, the following analysis was performed. The injection velocity parameter of Section 1 and the length of Section 2 are used as variables, so as to ascertain the conditions for which the Crestatron efficiency of Section 1 can be used to enhance the saturation efficiency at the TWT output.

The analysis is based on ending Section 1 at an axial position where a maximum Crestatron gain peak occurs, and calculating the saturation power $\left(P_{peak}\right)$ at the TWT output. Similarly, the saturation output power $\left(P_{null}\right)$ is computed for the case where Section 1 is adjusted to an axial position where a Crestatron gain null occurs. The saturation power difference $\left(P_{peak}/P_{null}\right)$ in dBm is determined. This procedure is performed for numerous Section 2 circuit lengths and Section 1 injection velocity parameters, and the results are presented in Fig. 11a. The output saturation efficiency that results when the length of Section 1 is adjusted to a maximum Crestatron gain peak is illustrated in Fig. 11b. The injection velocity parameter where x_1 converges to zero is $bl = 2.4$.

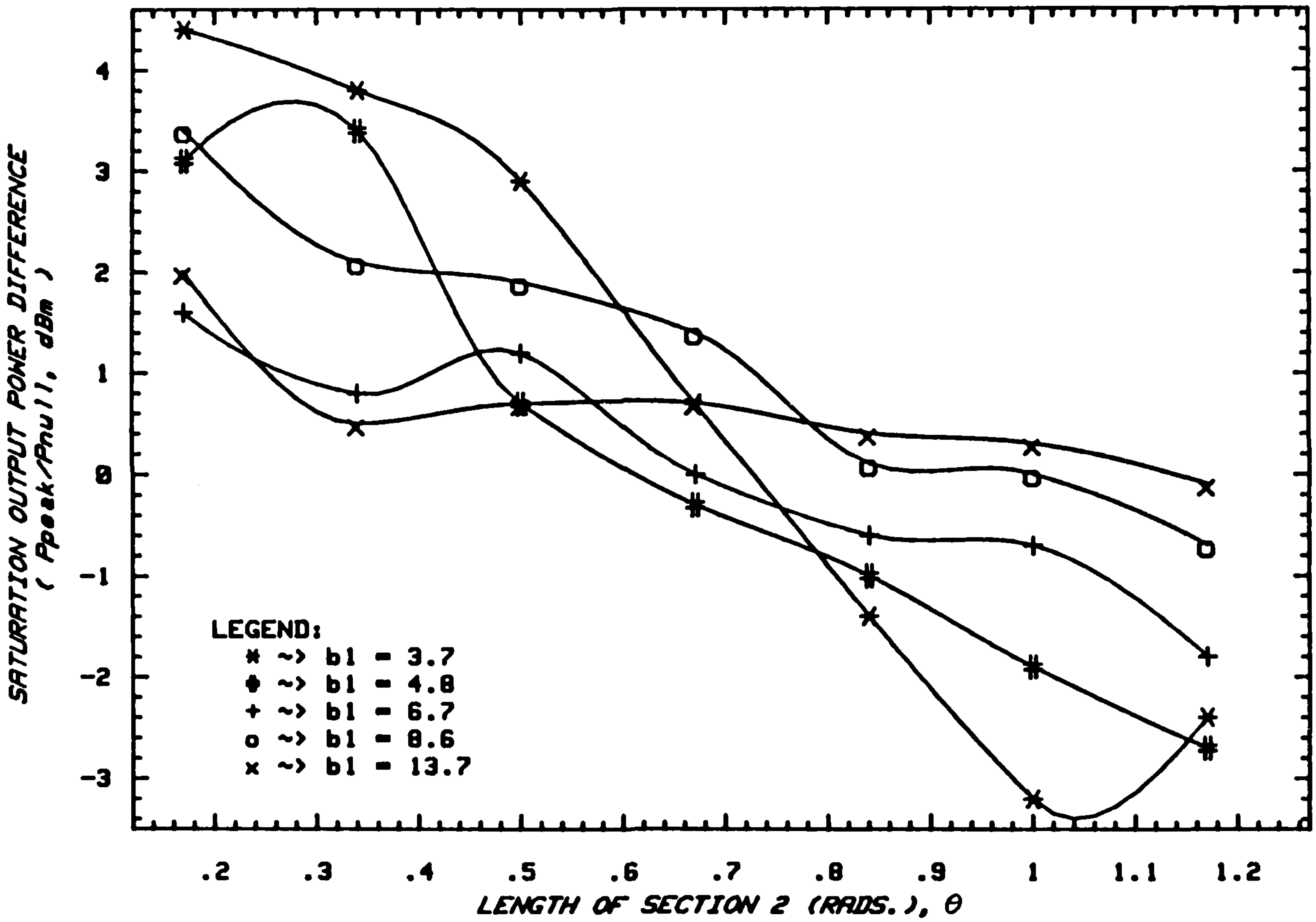

Fig. 11a. Saturation output power difference between ending Section 1 at a Crestatron gain peak and null (C1 = 0.105, b2 = 0.81, C2 = 0.086).

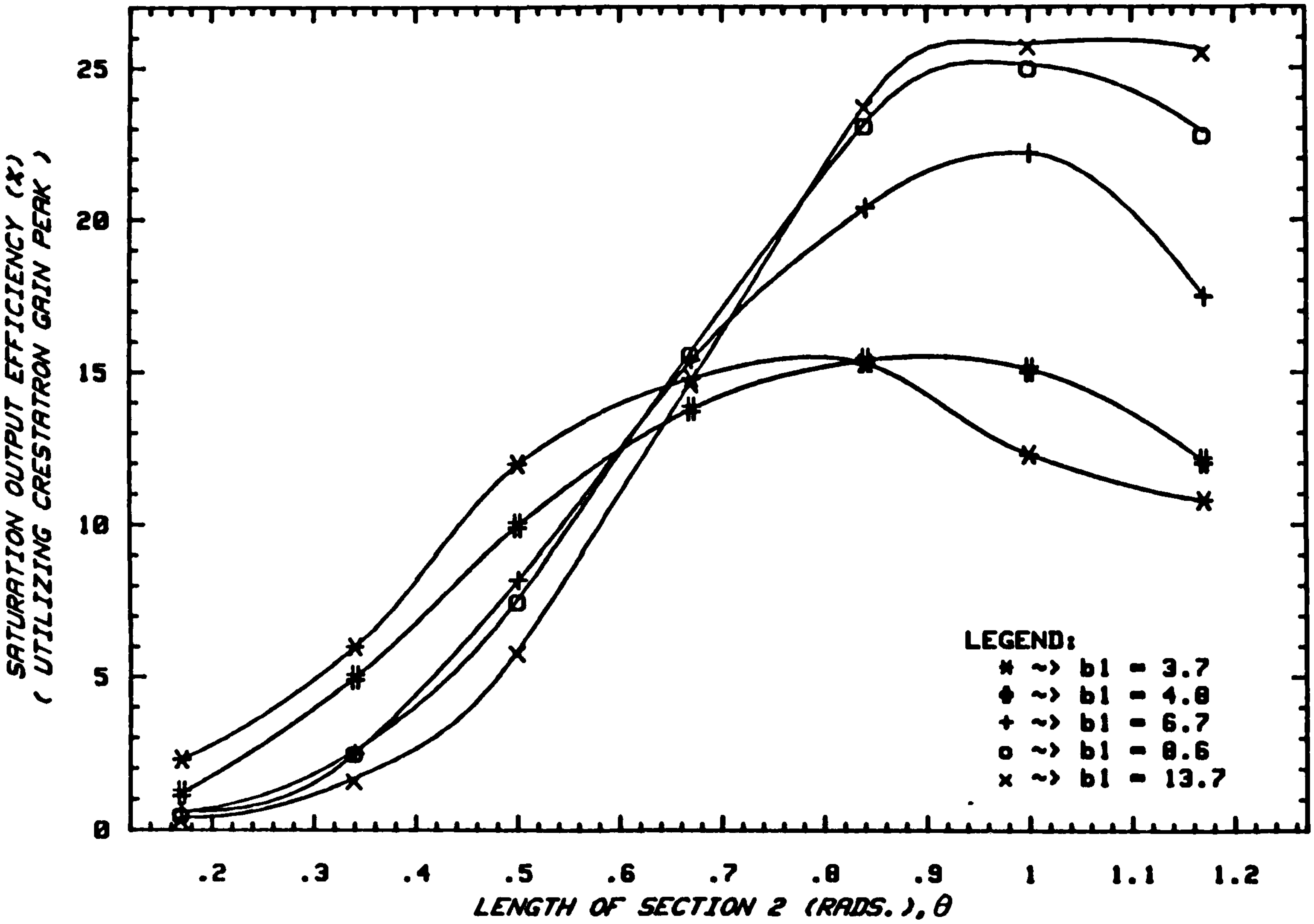

Fig. 11b. Saturation efficiency at the output due to utilizing the Crestatron gain peak occurring in Section 1 (C1 = 0.105, b2 = 0.81, C2 = 0.086).

Figures 11a and 11b display the power difference and saturation efficiency resulting from the utilization of the Crestatron gain peak occurring in Section 1 versus the radian length of Section 2. The figure shows that for a very short Section 2 circuit length (e.g., θ = 0.1 to 0.4 radians), the efficiency at the output is low even though utilization of the Crestatron effect enhances the TWT performance up to 4 dBm. As the length of Section 2 increases, utilization of the Crestatron interaction in Section 1 begins to degrade the TWT performance — the stronger the Crestatron interaction, the greater the degradation. An example of this is at θ = 1.0 radian. For a bl = 3.7, the output power is degraded by over 3 dBm, whereas for bl = 13.7, the Crestatron interaction has very little effect. Thus, the Crestatron efficiency of Section 1 enhances the tube's output efficiency for the cases where the circuit length of Section 2 is much shorter than the length which yields maximum efficiency.

Figures 12a and 12b display the degenerate influence a Crestatron gain peak can have on the beam-circuit wave interaction in Section 2. At approximately θ = 0.2, an electron bunch begins to form in a decelerating fundamental field region. The circuit wave amplitude reaches its maximum at θ = 0.6. The efficiency at this point is 15 percent. Because of the strong circuit fields and space-charge forces, the bunch begins to decay and is pushed into an accelerating fundamental field where the electrons begin to rebunch. This causes the circuit wave amplitude to decay, as shown in Fig. 12a. The resultant effect of the Crestatron efficiency in Section 1 is to force the TWT into premature saturation.

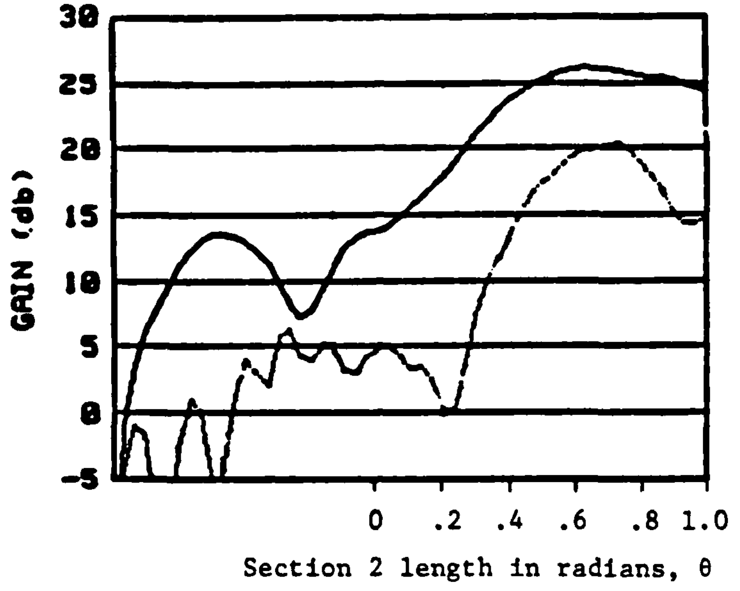

Fig. 12a. Utilizing Crestatron gain peak in Section 1 of the output circuit (b1 = 3.7, c1 = 0.104, b2 = 0.01, c2 = 0.086, ———— fundamental, - - - - - 2nd harmonic).

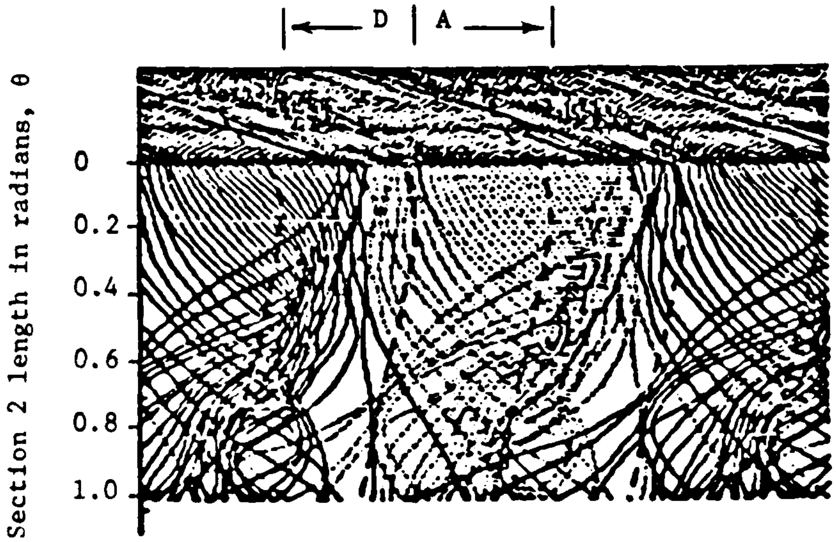

Fig. 12b. Phase trajectory versus Section 2 circuit length.

Figures 13a and 13b illustrate the TWT's performance when Section 1 is terminated at a Crestatron gain null. The circuit wave grows normally and achieves a much greater efficiency (24 percent) at the output. Figure 13b shows that an electron bunch forms at approximately $\theta = 0.3$ in a decelerating fundamental field region. The electrons remain bunched in this field region much longer than in the previous case. The circuit field grows until approximately $\theta = 0.9$. The bunch begins to collapse and saturation occurs. In Figs. 12b and 13b, prior to $\theta = 0.0$, the trajectory curves indicate that electron bunching does not occur, which is characteristic of the Crestatron interaction phenomenon.

Saturation Crestatron efficiencies result at much higher drive levels than in the normal growing wave case. The Crestatron interaction in Section 1 is a small signal phenomenon, even though the TWT is in saturation.

In the UBB design, Crestatron interaction occurs in Section 1 for middle and high band frequencies. Figures 11a and 11b indicate that maximum efficiencies resulting in this frequency range will be solely due to the normal forward circuit wave growth in Section 2. Using the Crestatron phenomenon might be feasible if the length of Section 2 is much shorter than the optimal length which maximizes the efficiency. Conversely, if the circuit length of Section 2 approaches the optimal length, a Crestatron gain peak occurring at the Section 1-Section 2 junction will cause the normal circuit wave growth in Section 2 to degenerate if the Crestatron interaction is strong enough. As the frequency increases, the injection velocity parameter bl increases in

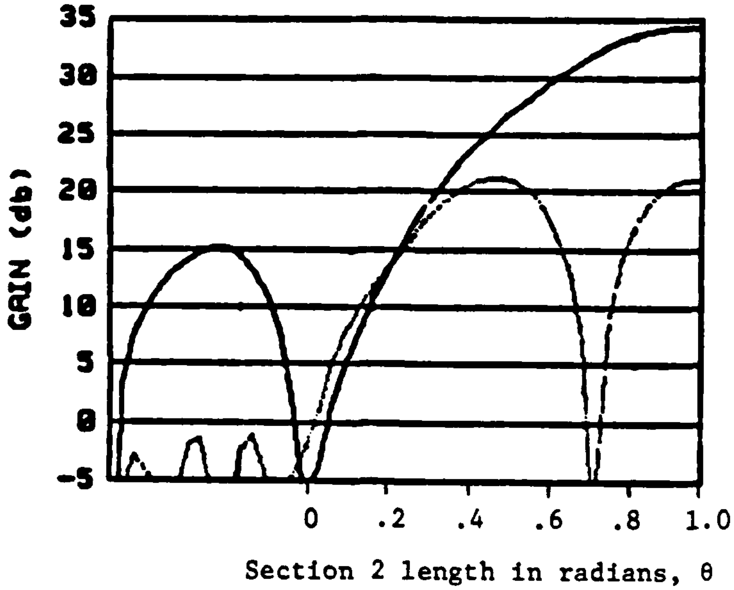

Fig. 13a. Utilizing Crestatron gain null in Section 1 of output circuit (bl = 3.7, cl = 0.104, b2 = 0.81, c2 = 0.086, ——— fundamental, - - - - 2nd harmonic).

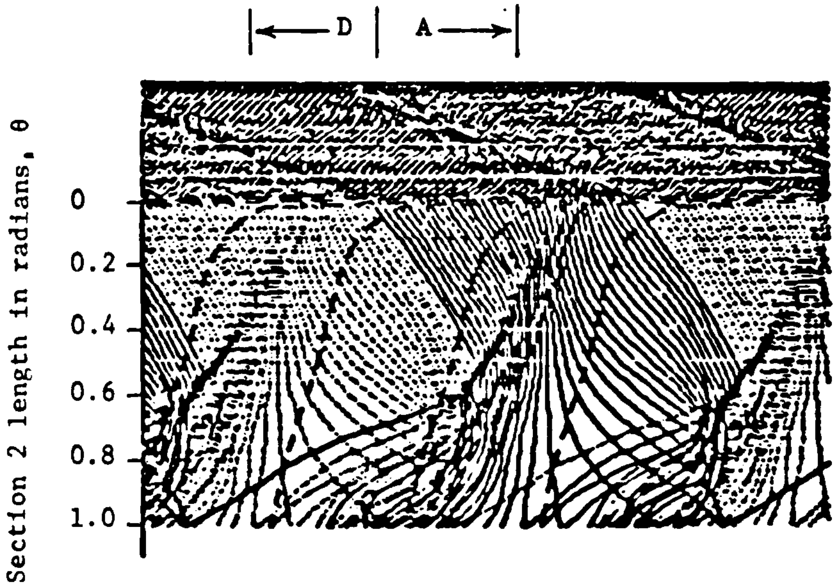

Fig. 13b. Phase trajectory versus Section 2 circuit length.

value, and the effect of the Crestatron interaction phenomenon on Section 2 lessens and becomes negligible at the high end of the band.

Utilizing the Crestatron interaction in Section 1 at multiple frequencies is limited, since the axial location of the Crestatron gain peaks and nulls are extremely sensitive to the variation in the injection velocity parameter and the input drive level. Also, the circuit length of Section 2 for which the maximum saturation efficiency results varies with frequency and the injection velocity parameter.

D. Output Circuit Length Ratio Analysis

This analysis is based on varying the length of Section 1, and calculating the efficiency and harmonic suppression as a function of this variation. The lengths of Section 1 and 2 are adjusted accordingly, so that the overall output circuit length remains constant. The electrical characteristics of Section 1 and 2 are listed in Table 1.

Table 1. Table of electrical parameters which characterize Sections 1 and 2 of the output circuit with respect to the circuit length ratio analysis.

f	b1	C1	b2	C2
2	1.28	0.122	1.055	0.096
3	1.80	0.121	0.98	0.094
5	2.95	0.114	0.85	0.088
9	5.40	0.084	0.84	0.076
13	8.80	0.059	1.23	0.062
18	12.20	0.044	2.04	0.049

The TWT performance as a function of the dispersiveness and length of Section 1 at f = 2 GHz is displayed in Figs. 14a and 14b. The length of Section 1 (θ_1) is expressed in radians, where

$\theta_1 = 2\pi$ Cl Ng

Cl = Section 1 gain parameter

Ng = number of undisturbed wavelengths = f/c L1

Figure 14a indicates that as Vh/Vf is increased, maximum harmonic suppression occurs for an increased θ_1. The reason is because, as the velocity ratio increases in value, the farther the second harmonic component of the circuit wave must propagate before the second harmonic circuit field undergoes the necessary phase shift for harmonic suppression. If Vh/Vf is too great a value, the harmonic will dominate and force the fundamental into premature saturation before the minimum phase shift for harmonic suppression can occur. Maximum suppression results when the second harmonic circuit field undergoes a π radian phase shift (second harmonic phase units) relative to the fundamental circuit field at the Section 1-Section 2 junction. This phenomenon is displayed in Figs. 15a and 15b.

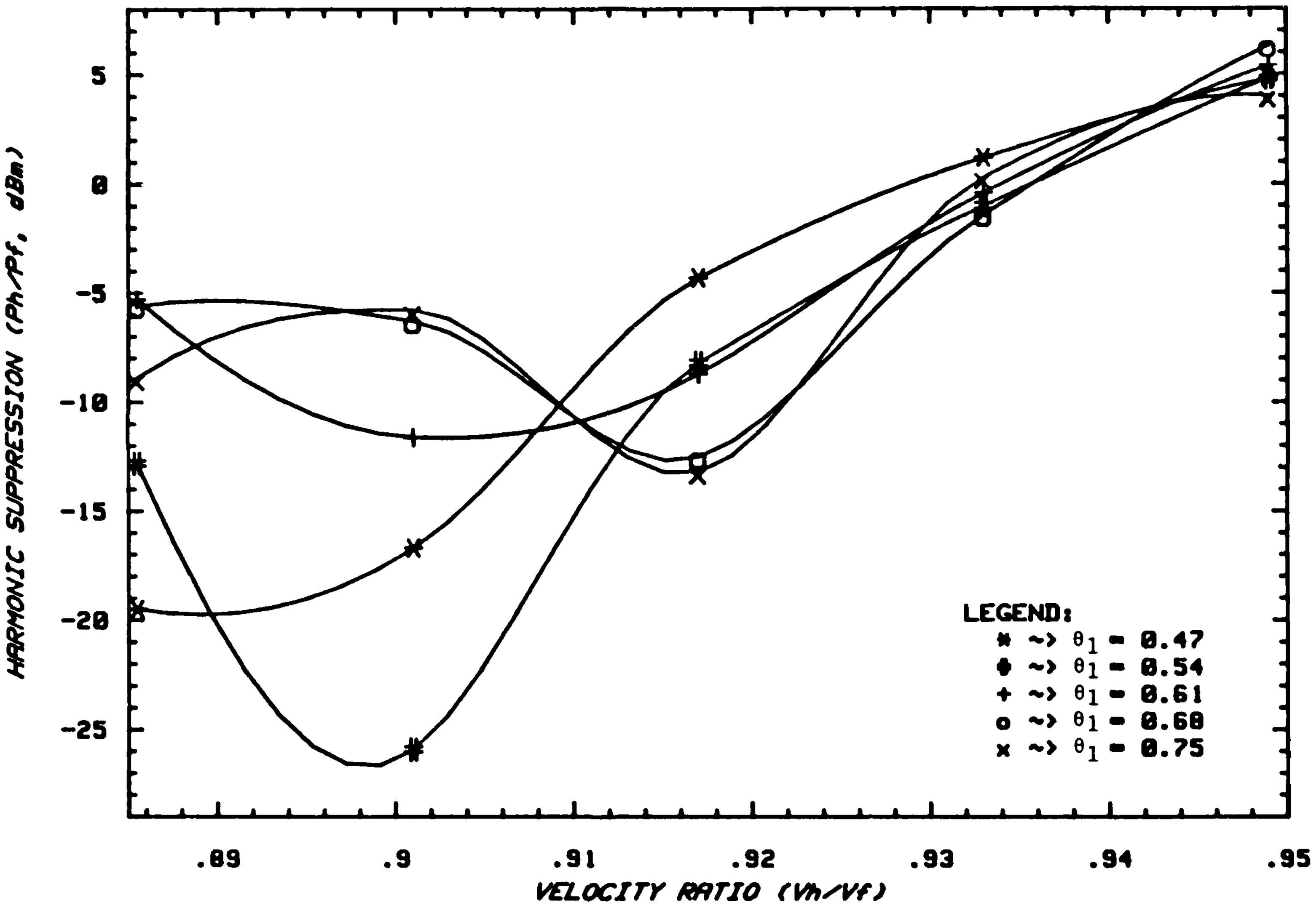

Fig. 14a. Second harmonic suppression as function of phase velocity ratio and Section 1 length (rads) (F = 2 GHz, b1 = 1.28, C1 = 0.122, b2 = 1.055, C2 = 0.096).

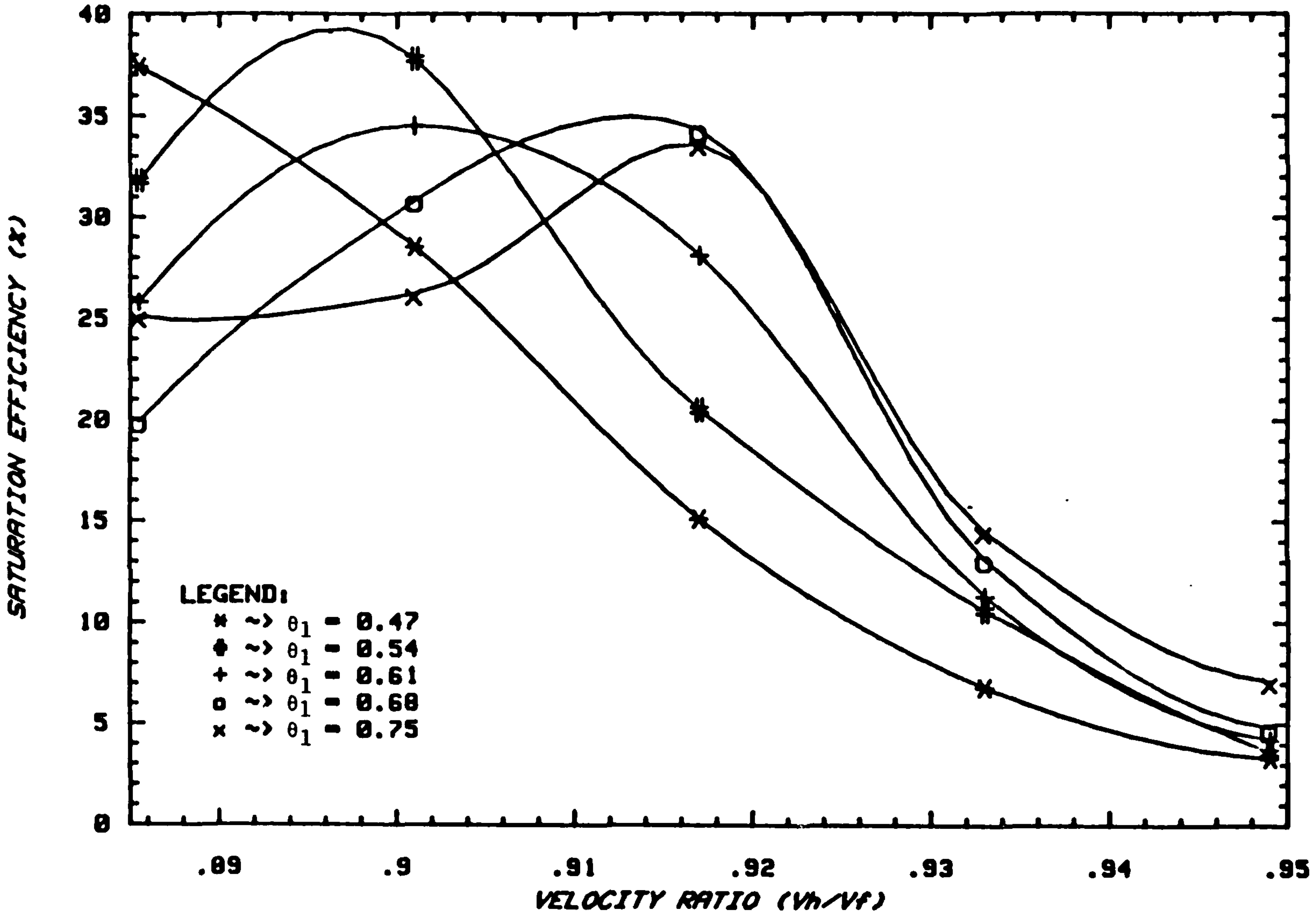

Fig. 14b. Saturation efficiency as function of phase velocity ratio and Section 1 length (rads) (F = 2 GHz, b1 = 1.28, C1 = 0.122, b2 = 1.055, C2 = 0.096.

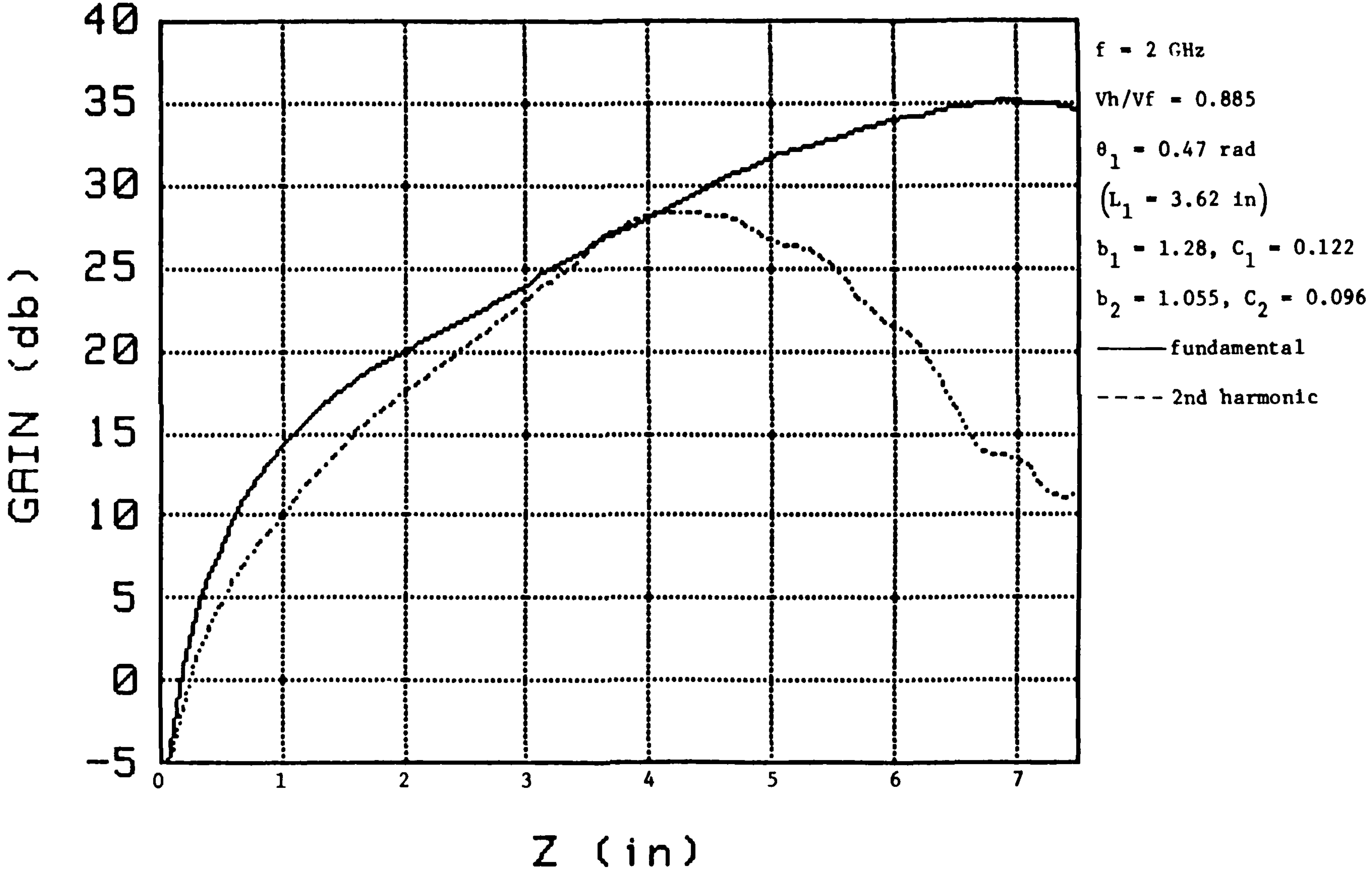

Fig. 15a. Gain versus output circuit length.

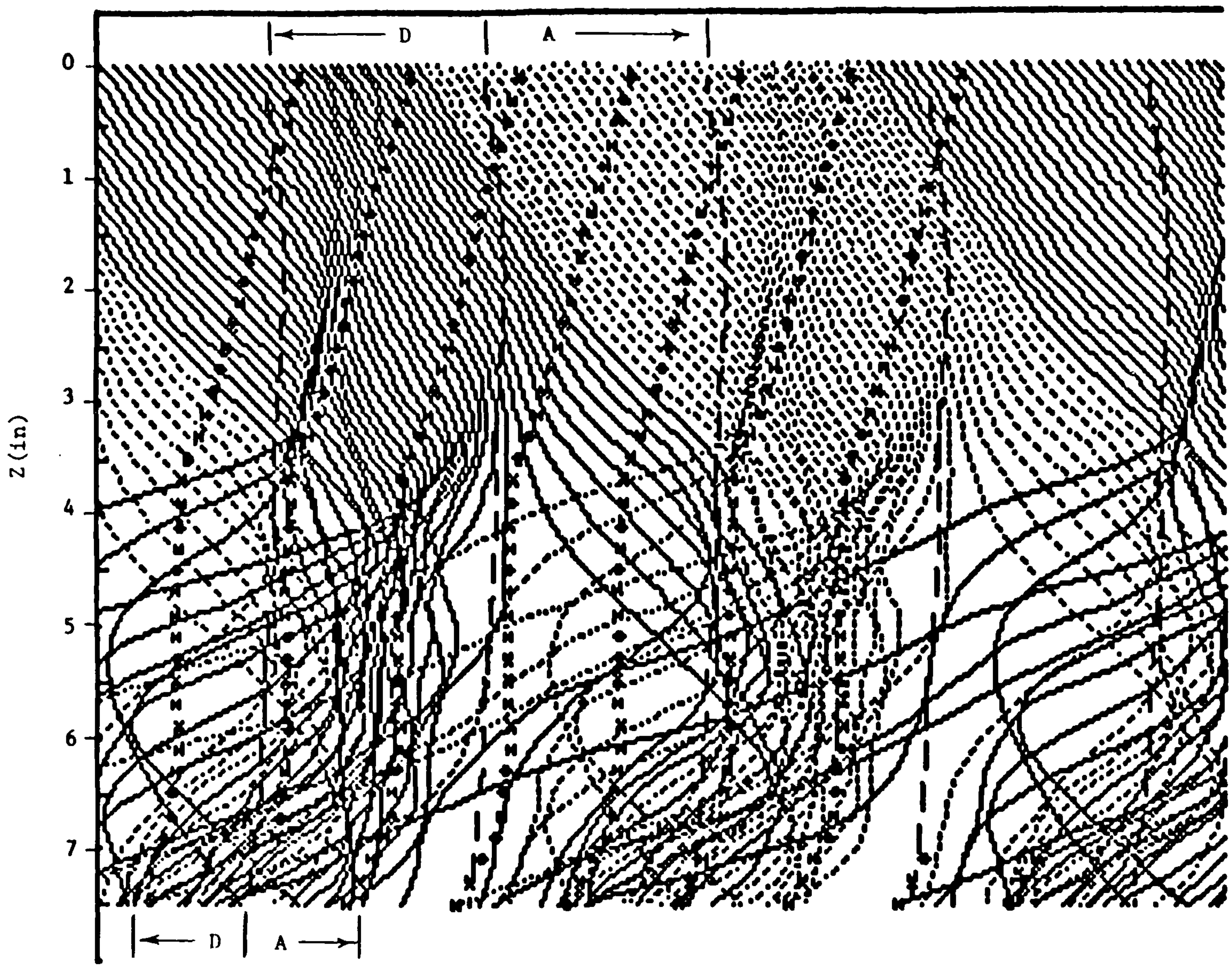

Fig. 15b. Phase trajectory versus output circuit length.

At the Section 1-Section 2 junction, the second harmonic circuit field has undergone a phase shift that is slightly greater than π radians. The bunching electrons occur within an accelerating second harmonic circuit field region, as shown in Fig. 15b. Figure 15a displays the gain of the forward circuit wave and illustrates that the second harmonic component has been thoroughly suppressed. If the length of Section 1 is increased, the second harmonic circuit field will undergo too great a phase shift and the bunching electrons will eventually converge into a decelerating harmonic circuit field region. An example of this phenomenon is illustrated in Figs. 16a and 16b. The bunching electrons initially occur within an accelerating harmonic circuit field region. Because of the extreme dispersiveness (Vh/Vf = 0.885) and length $(\theta_1 = 0.67)$ of Section 1, the accelerating harmonic circuit field region shifts past the electron bunch at z = 4.9, which results in a decelerating harmonic circuit field region coinciding with the bunching electrons. The second harmonic again begins to grow, as shown in Fig. 16a.

In Figs. 14a and 14b, maximum harmonic suppression and efficiency enhancement occur for Vh/Vf = 0.901. The data plots illustrated in Figs. 17a and 17b are based on this velocity characteristic. Harmonic suppression at selected frequencies in the lower half of the band and saturation efficiency across the entire bandwidth are presented as a function of the length ratio L1/Lt. The figures show that the ratio L1/Lt = 0.55 yields the best cumulative result across the band. Figure 17b indicates that as the length ratio increases in value, the efficiency for frequencies in the upper half of the band decreases. The gain

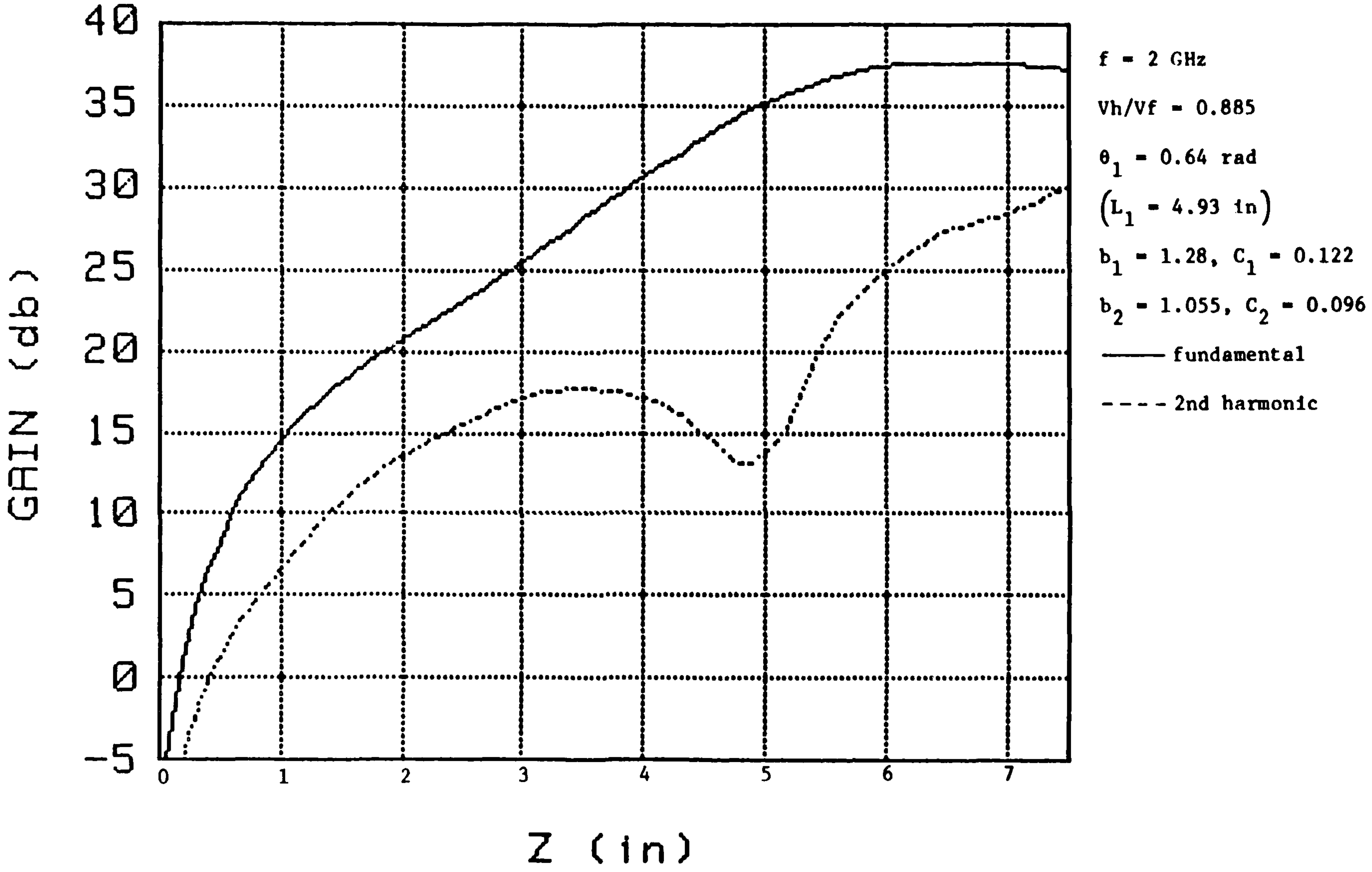

Fig. 16a. Gain versus output circuit length.

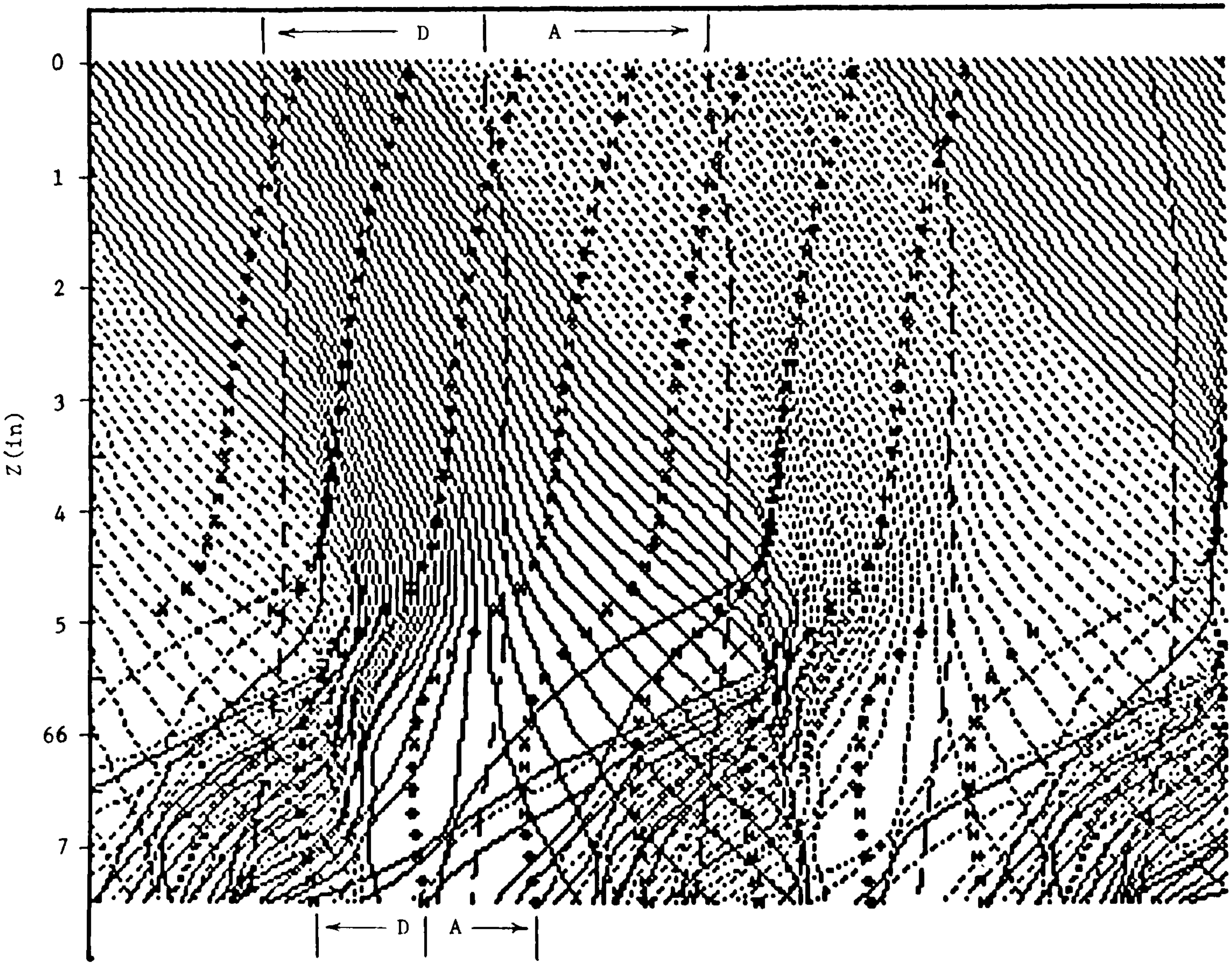

Fig. 16b. Phase trajectory versus output circuit length.

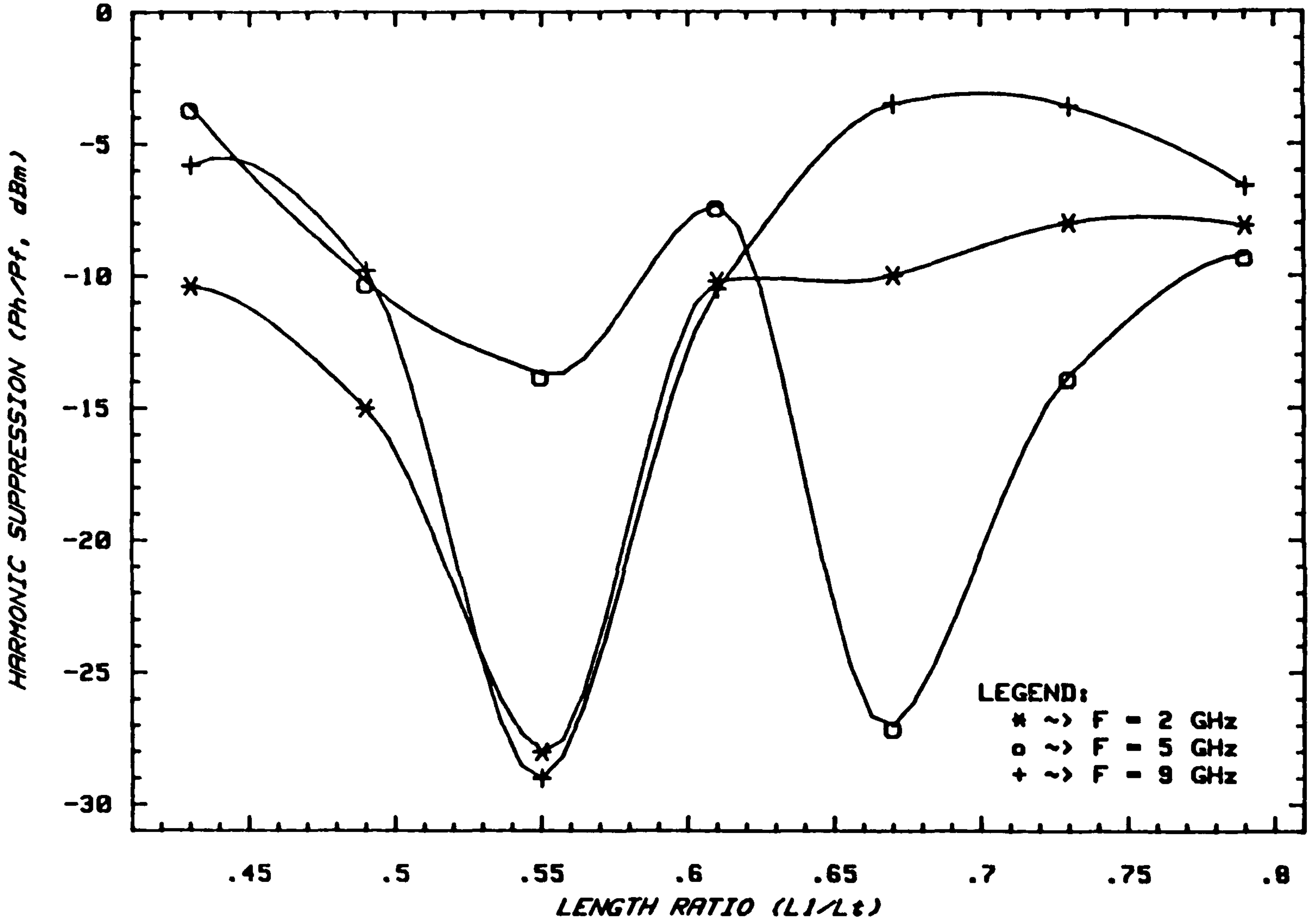

Fig. 17a. Second harmonic suppression as a function of the length ratio. (Vh/Vf = 0.90 at F = 2 GHz, Table 1 lists b's and C's).

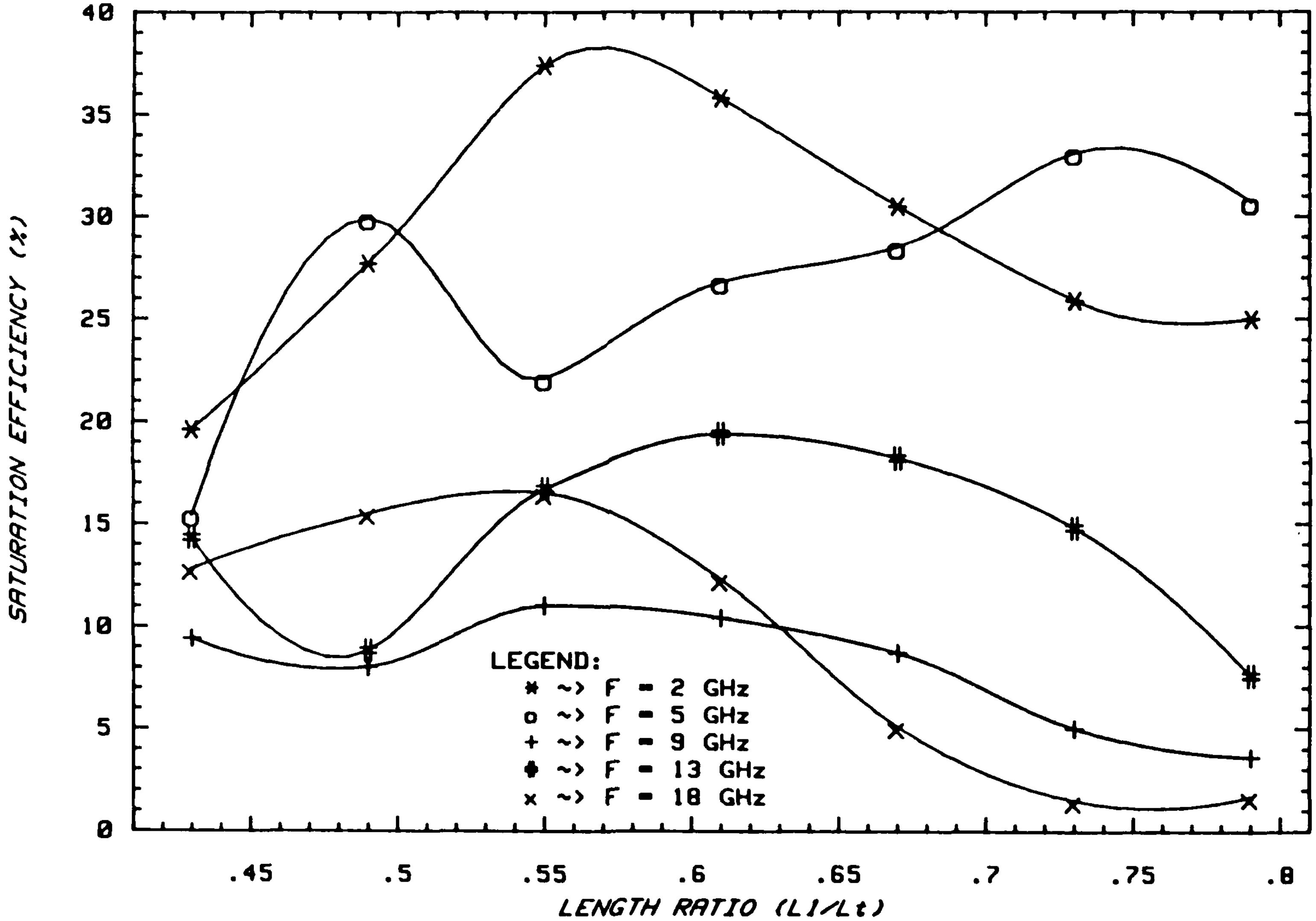

Fig. 17b. Saturation efficiency as function of the length ratio (Vh/Vf = 0.90 at F = 2 GHz, Table 1 lists b's and C's).

that occurs in this frequency region is solely due to the normal growing wave interaction in Section 2. If the length of Section 2 is set at too small a value, the efficiency at the high end of the band will be diminished.

E. Theoretical Design

A theoretical output circuit design, based on the TWT operating conditions specified in Chapter 2, is presented in this section. The velocity characteristics of the output circuit are shown in Fig. 18. The dispersion of Section 1 has been designed so that maximum harmonic suppression is obtained at f = 2 GHz. The dispersion of Section 2 has been designed to optimize the efficiency across the 2-18 GHz bandwidth. The velocity characteristics of this section are slightly different from those presented in Fig. 6a. The phase velocity at midband has been decreased by approximately 1.3 percent in order to increase the efficiency in this sector of the band. The phase velocity crossover frequency is roughly 1.5 GHz, and the output circuit length ratio is Ll/Lt = 0.55. The electrical parameters which characterize the design under operating conditions are listed in Table 2. Figures 19a and 19b display the TWT theoretical performance. The figures show that the saturation efficiency of the fundamental circuit wave ranges between 15 and 30 percent across the 2-18 GHz band. The minimum separation between the fundamental and second harmonic is 4.5 dBm at midband. Greater efficiency and harmonic suppression at midband could possibly be obtained by tweeking L_1/L_t.

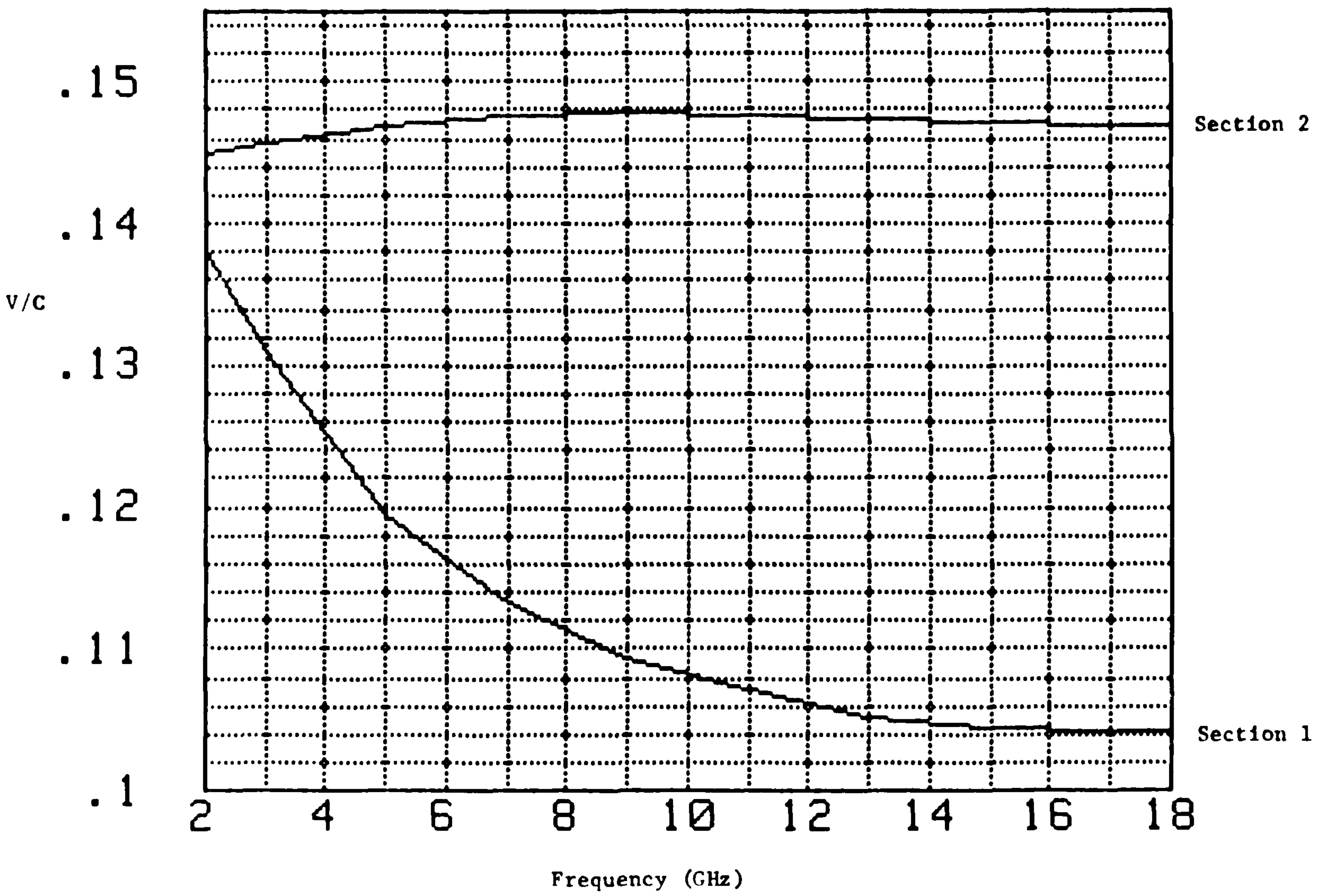

Fig. 18. Dispersion of output circuit for a 3.2 octave bandwidth theoretical design (u_o/c = 0.1597, 0.14 μp).

Table 2. Electrical parameters which characterize a 3.2 octave bandwidth theoretical design.

f(GHz)	b1	C1	b2	C2
2	1.28	0.123	1.06	0.095
3	1.8	0.122	1.04	0.093
5	2.95	0.114	1.01	0.087
7	4.1	0.100	1.02	0.081
9	5.4	0.084	1.09	0.074
11	7.0	0.070	1.22	0.067
13	8.8	0.059	1.39	0.060
15	10.5	0.051	1.6	0.053
17	11.6	0.046	1.85	0.047
18	12.1	0.044	1.98	0.044

Up to this point, very little has been mentioned about the input circuit of the ultrabroadband TWT. One main consideration is to design the input circuit for maximum gain flatness. Reducing the gain expansion between the middle and band edge frequencies will improve the tube's noise figure, thus resulting in a cleaner amplified RF signal at the TWT output.

Another design guideline is that the signal level at the sever should be low compared to the satauration level so that the nonlinear effects and velocity spread are small as the beam enters the output circuit. A signal level that is high at the sever results in a large velocity spread in the beam at the sever termination. The greater the velocity spread, the shorter the lifetime of the electron bunches, and

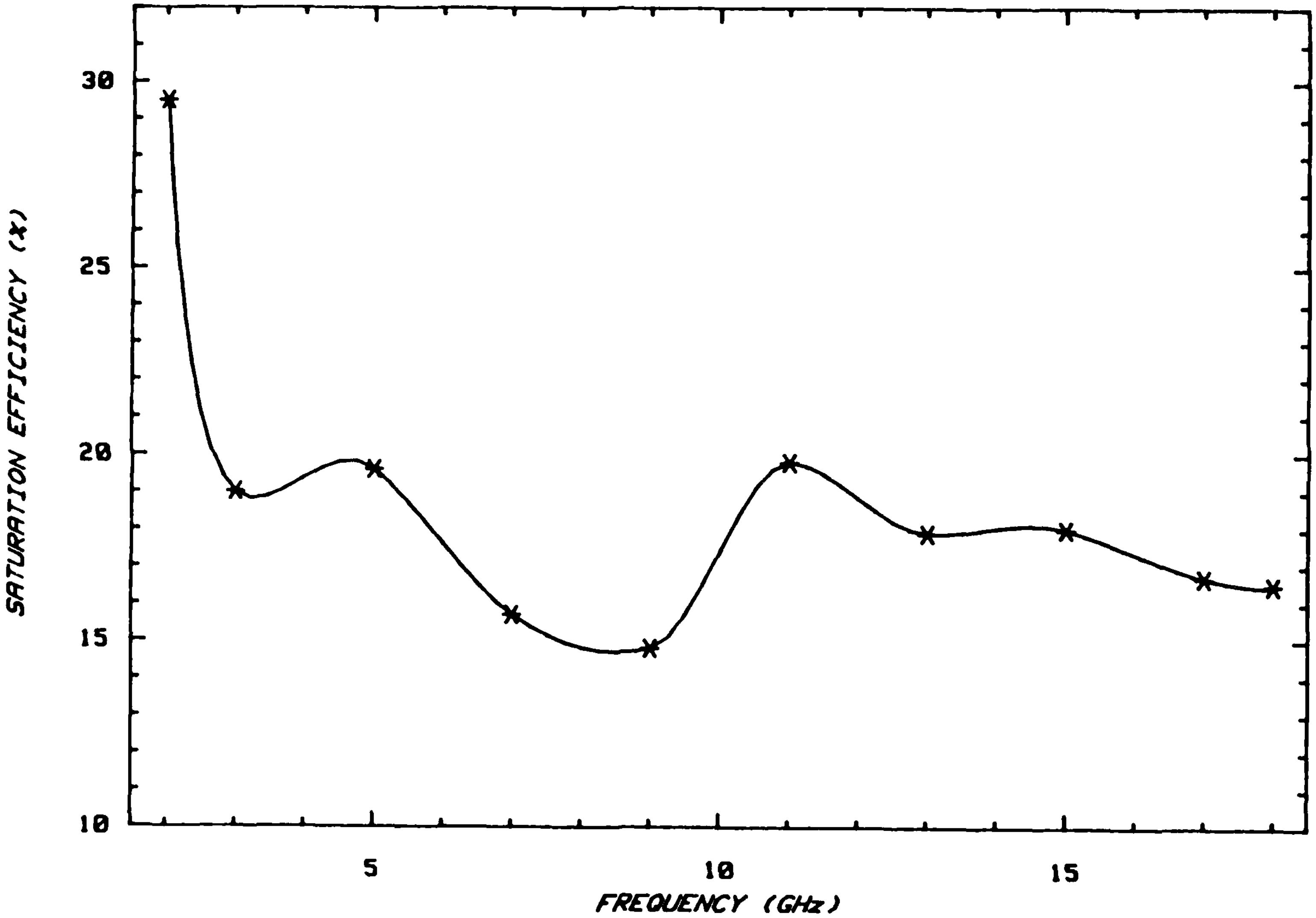

Fig. 19a. Theoretical efficiency performance of a 3.2 octave bandwidth output circuit design (see Fig. 18 and Table 2 for electrical parameters).

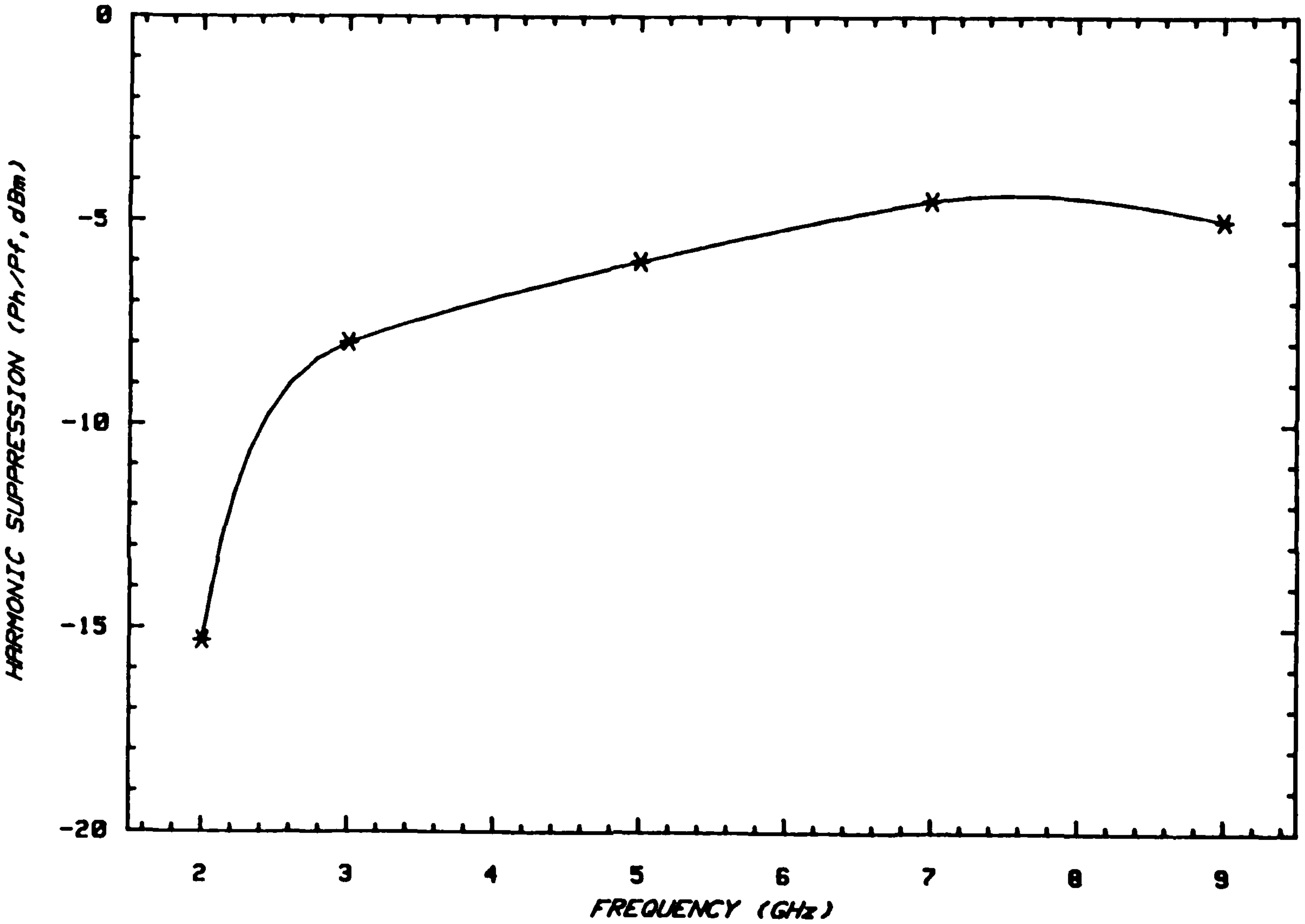

Fig. 19b. Theoretical 2nd harmonic suppression for a 3.2 octave bandwidth output circuit design (see Fig. 18 and Table 2 for electrical parameters).

the kinetic energy transfer from the beam to the circuit wave is reduced. Scott[22] has shown that the debunching of the beam by space-charge forces in the region between the sever and the point where the signal builds up to the value it previously reached at the sever is the cause for the reduction in the saturation output signal. The minimum small signal gain in the output circuit necessary to prevent a serious reduction in efficiency is at least 26 dB.

VI. SUMMARY AND CONCLUSIONS

The scope of this report has been concerned with determining the design considerations for a helix-type TWT output circuit which will yield a 2-18 GHz operating bandwidth. The primary focus has been to determine the conditions necessary to enhance the band edge performance at f = 2 GHz. The output circuit consists of two sections. The results are based on one-dimensional large signal TWT computer simulations.

The main criterion in achieving a 3.2 octave bandwidth is to design the dispersion and length of Section 1 so that the second harmonic circuit field is phase focussed for maximum harmonic suppression at the low frequency band edge. The numerical results indicated that the degree of harmonic suppression is extremely sensitive to the dispersiveness of this section. For maximum harmonic suppression to occur, the second harmonic component of the circuit field must undergo a π radian phase shift (second harmonic phase units) relative to the fundamental at the Section 1-Section 2 junction. At f = 2 GHz and a microperveance equal to 0.14, this phenomenon occurs for a phase velocity ratio $V_h/V_f = 0.90$ and a circuit length $\theta_1 = 0.54$ radians. The velocity profile of Section 1 has a dispersion factor $D_f = 0.192$.

The velocity characteristics and length of Section 2 must be designed so that the efficiency across the band is optimized. A velocity profile displaying negative-to-flat dispersion will yield the synchronism that is necessary for normal forward circuit wave growth at all frequencies in the band. The length of Section 2 should be set at a value which maximizes the efficiency.

The range of the injection velocity parameter for Sections 1 and 2, which yield maximum saturation efficiencies at f = 2 GHz, is $1.2 < b1 < 1.6$ and $0.78 < b2 < 1.33$.

For some TWT designs, stability constraints (e.g., BWO due to excessive length) could cause the length of Section 2 to be reduced. Utilization of the Crestatron efficiency occurring in Section 1 might become feasible for such a case. The length of Section 1 would have to be set at a value which utilizes the Crestatron phenomena. Conversely, if the length of Section 2 is relatively long, a Crestatron efficiency peak occurring at the Section 1-Section 2 junction will degrade the efficiency at the output. Incorporating Crestatron efficiency in the design is very limited, since the axial position of a Crestatron peak or null varies with the injection velocity parameter, input drive level, and frequency.

The results of this study have shown that a TWT can theoretically achieve a 3.2 octave bandwidth. Suggestions for further studies are to determine whether the dispersion characteristics of the output circuit can be physically realized, and to build and test a helix TWT based on these theoretical concepts. Also, further work must include studies which determine methods for eliminating TWT instabilities (e.g., BWO and gain ripple) which are prevalent in TWTs that operate over multioctave bandwidths.

REFERENCES

1. P. L. Walchli, "Multiple Octave Traveling-Wave Tubes," *IEDM Technical Digest*, 1981, p. 697.

2. J. P. Rymer and M. J. Cascone,"Three Octaves with One TWT," *IEDM Technical Digest*, 1982, pp. 30-31.

3. H. Frerking, L. Lav, and D. Zavadil, "Velocity Dispersion Shaping for Helix TWT Improvement," *IEDM Technical Digest*, 1974, p. 487.

4. G. S. Kino, "Normal Mode Theory in Perturbed Transmission Systems," Technical Report 84, Electronics Research Laboratory, Stanford University, Stanford, California, May 1955.

5. A. Scott and M. J. Cascone, "What's New in Helix TWTs?" *IEDM Technical Digest*, 1978, p. 526.

6. J. L. Putz, A. Scott, and M. J. Cascone, "Evaluation of Phase Velocity Dispersion Control," Final Report of NRL Contract No. N00173-77-C-0301, November 1979.

7. P. L. Walchli, "T-Helix Technology," Final Report of NRL Contract No. N00173-79-C-0050, November 1981.

8. J. R. Pierce, *Traveling-Wave Tubes*, D. Van Nostrand Company, New York, 1950.

9. J. E. Rowe, "Theory of the Crestatron: A Forward-Wave Amplifier," *Proceedings of the IRE*, April 1959, pp. 536-545.

10. J. L. Putz, "Nonlinear Behavior of Traveling-Wave Amplifiers," Technical Report No. 37, Electronics Research Laboratory, Stanford University, Stanford, California, October 15, 1951.

11. R. L. Baer, "Harmonic Injection in Helix Type Traveling-Wave Tubes," AFTER Thesis submitted to the Electrical Engineering Department, Stanford University, Stanford, California, March 198[illegible].

12. N. J. Dionne, "Harmonic Generation in Octave Bandwidth Traveling-Wave Tubes," *IEEE Transactions on Electron Devices*, Vol. ED-17, April 1970, pp. 365-372.

13. A. J. Sangster, "Traveling-Wave Interaction in Structures with Nonzero Impedance at Harmonics of the Drive Frequency," *Proceedings of the 6th International Conference on Microwave and Optical Generation and Amplification*, September 1966, pp. 125-13[illegible].

14. S. F. Paik, "Design Formulas for Helix Dispersion Shaping," IEEE Transactions on Electron Devices, Vol. ED-16, December 1969, pp. 1010-1014.

15. P. K. Tien, "A Large Signal Theory of Traveling-Wave Amplifiers," Bell System Technical Journal, March 1956, pp. 349-374.

16. R. C. Moorwood, "A Computer Program for Large Signal Analysis of a TWT with Helix-Type Circuits," Varian Tube Division Memorandum TDM-54, April 1969.

17. S. Wallander, "Large Signal Computer Analysis of Klystron Waves," International Journal of Electronics, Vol. 24, No. 2, 1968, pp. 185-196.

18. S. Ramo and J. R. Whinnery, Fields and Waves in Modern Radio, Second Edition, John Wiley and Sons, Inc., New York, 1953.

19. S. Olving and S. Wallander, "Nonlinear Space-Charge Wave Theory of the Hydrodynamic Disk-Electron Beam," Research Report No. 42, Research Laboratory of Electronics, Chalmeis University of Technology, Gothenburg, Sweden, 1964.

20. J. L. Putz, "Helix Large Signal Computer Programs," Varian Associates Interoffice Report, October 13, 1981.

21. C. K. Birdsall and F. M. Schumacher, "Plasma Frequency Reduction in Electron Streams by Helices and Drift Tubes," IRE Transactions on Electron Devices, Vol. ED-6, October 1959, pp. 468-469.

22. A. W. Scott, "Why a Circuit Sever Affects Traveling-Wave Tube Efficiency," IRE Transactions on Electron Devices, Vol. ED-9, January 1962, p. 35.

APPENDIX A

DISPERSION FACTOR ANALYSIS

The data points in Fig. 7b display a linear variation within the range $-0.15 < dF < 0.15$. To determine whether this variation remains linear as the dispersion factor increases beyond 0.15, the effect of several geometric parameters must be investigated — the angle θ, the ratio b/a, and the ratio c/a. Figures A.1 and A.2 define these parameters.

The geometries shown in Figs. A.1 and A.2 were chosen because a relatively simple analysis can be performed in order to determine the effect of these parameters on the dispersion and interacting impedance. An analytical technique, based on equivalent circuit parameters derived from rigorous field analyses, was presented by Paik.[14] This technique uses transmission line theory to model the sheath helix as a lossless line with a series inductance per unit length, L, and a shunt capacitance per unit length, C. The propagation constant and characteristic impedance are defined as

$$\beta = \omega\sqrt{LC} \qquad (A.1)$$

$$Z_o = \sqrt{L/C} \qquad (A.2)$$

The impedance given by Eq. A.2 is equivalent to the transverse impedance [illegible] by Pierce.[8] Since this analysis is concerned only with the [illegible] dispersion variation, the following analysis will be left in [illegible] parameter.

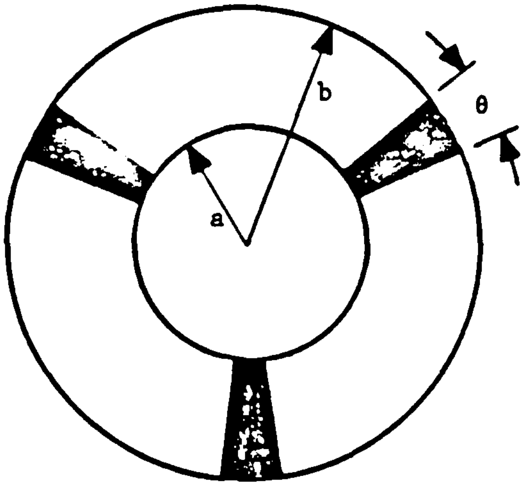

Fig. A.1. Sheath helix with shield and dielectric support rods.

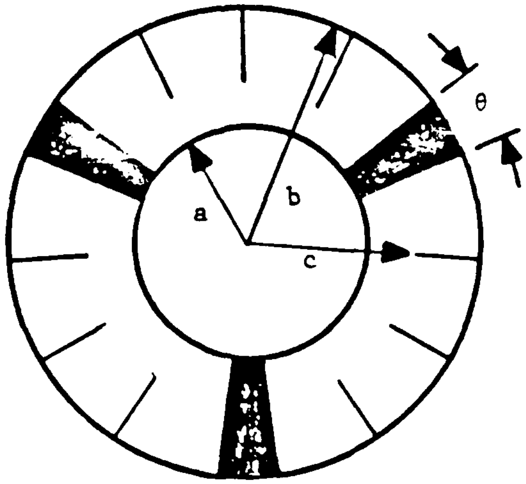

Fig. A.2. Sheath helix swith shield, metal fins, and dielectric support rods

Paik defines the shunt capacitance and series inductance for a circuit with the geometry shown in Fig. A.1 to be

$$C = C_o\left[1 + \left((\varepsilon_r)_{eff} - 1\right) \cdot D(\gamma a)\right] \cdot \left[1 - K_c^2(\gamma a, \gamma b)\right]^{-1} \tag{A.3}$$

$$L = L_o\left[1 - K_c^2(\gamma a, \gamma b)\right]$$

where

$$C_o = \frac{2\pi\varepsilon_o}{I_o(\gamma a)K_o(\gamma a)}$$

$$L_o = \left(\frac{\mu}{2\pi}\right)\left(\frac{\beta}{\gamma}\right)^2 \cot^2\psi\ I_1(\gamma a)K_1(\gamma a)$$

$$D(\gamma a) = (\gamma a)I_o(\gamma a)K_1(\gamma a)$$

$$K_c^2(\gamma a, \gamma b) = I_o(\gamma a)K_o(\gamma b)/I_o(\gamma b)K_o(\gamma a)$$

$$K_c^2(\gamma a, \gamma b) = I_1(\gamma a)K_1(\gamma b)/I_1(\gamma b)K_1(\gamma a)$$

$$(\varepsilon_r)_{eff} = 1 + \left(\theta \circ \frac{N}{2\pi}\right)(\varepsilon_r - 1)$$

N = number of dielectric wedges

The assumption $\beta = \gamma$ is made in order to simplify the following expressions. The pitch angle ψ is set equal to 0.1 radian so that $v/c \ll 1$. Making the appropriate substitutions into Eqs. A.3 and and A.4, and using the definitions

$$\omega/c = \omega\sqrt{\varepsilon\mu}$$

$$\beta = \frac{\omega}{v}$$

Eqs. A.1 and A.2 simplify to

$$v = c \tan\psi \left\{ \frac{I_o(\gamma a)K_o(\gamma a)}{I_1(\gamma a)K_1(\gamma a)} \; \frac{1 - \dfrac{I_o(\gamma a)K_o(\gamma b)}{I_o(\gamma b)K_o(\gamma a)}}{1 - \dfrac{I_1(\gamma a)K_1(\gamma b)}{I_1(\gamma b)K_1(\gamma a)}} \left[1 + \frac{\theta\ N}{2\pi}(\varepsilon_r - 1)(\gamma a)I_o(\gamma a)K_1(\gamma a)\right]^{-1} \right\}^{1/2} \qquad (A.5)$$

$$Z_o = \frac{\cot\psi}{2\pi}\sqrt{\frac{\mu}{\varepsilon_o}} \left\{ \frac{I_1(\gamma a)K_1(\gamma a)I_o(\gamma a)K_o(\gamma a)}{\left[1 + \left(\dfrac{\theta\ N}{2\pi}\right)(\varepsilon_r - 1)(\gamma a)I_o(\gamma a)K_1(\gamma a)\right]} \left[1 - \frac{I_1(\gamma a)K_1(\gamma b)}{I_1(\gamma b)K_1(\gamma a)}\right]\left[1 - \frac{I_o(\gamma a)K_o(\gamma b)}{I_o(\gamma b)K_o(\gamma a)}\right] \right\}^{1/2} \qquad (A.6)$$

Equations A.5 and A.6 were used to create the plots shown in Fig. A.3. The plots show that the impedance-dispersion factor variation is nonlinear as the shield-to-helix diameter ratio is varied between 1.3 and 2.46. For low values of Df, the variation is seen to be linear, but as the dispersion factor increases, the relationship becomes nonlinear.

According to Paik, the shunt capacitance for a circuit with the geometry shown in Fig. A.2 is also expressed by Eq. A.2. The series inductance is defined as

$$L = L_o\left(1 - k_\ell^2(\gamma a,\ \gamma c)\right)$$

where

$$k_\ell^2(\gamma a,\ \gamma c) = I_1(\gamma a)K_1(\gamma c)/I_1(\gamma c)K_1(\gamma a)$$

Using the assumption $\beta \approx \gamma$, and making the appropriate substitutions, Eqs. A.1 and A.2 simplify to

$$v = c_1\ \tan\psi \left\{ \frac{I_o(\gamma a)K_o(\gamma a)}{I_1(\gamma a)K_1(\gamma a)}\ \frac{1 - \dfrac{I_o(\gamma a)K_o(\gamma c)}{I_o(\gamma c)K_o(\gamma a)}}{1 - \dfrac{I_1(\gamma a)K_1(\gamma b)}{I_1(\gamma b)K_1(\gamma a)}} \right.$$

$$\left. \left[1 - \left(\frac{\theta \cdot N}{2\pi}\right)(\varepsilon_r - 1)(\gamma a)I_o(\gamma a)K_1(\gamma c)\right]^{-1} \right\}^{1/2} \qquad \text{(A.7)}$$

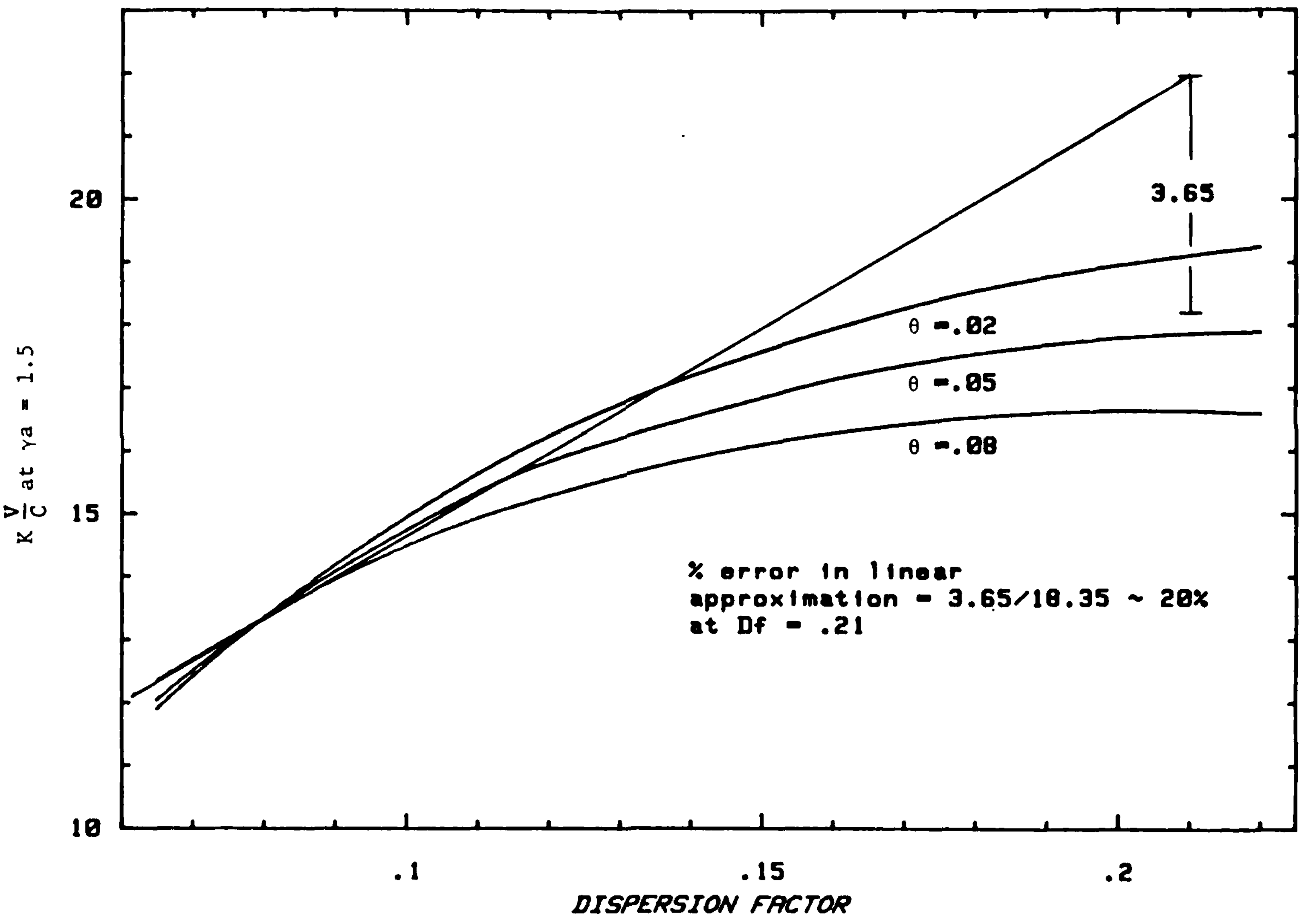

Fig. A.3. Impedance variation versus the dispersion factor ($\psi = 0.1$, $\varepsilon_r = 5$, $N = 3$, $1.30 < b/a < 2.46$).

$$Z_o = \frac{\cot \psi}{2\pi} \sqrt{\frac{\mu}{\varepsilon_o}} \left\{ \frac{I_1(\gamma a)K_1(\gamma a)I_o(\gamma a)K_o(\gamma a)}{1 + \left(\frac{\theta \cdot N}{2\pi}\right)(\varepsilon_r - 1)(\gamma a)I_o(\gamma a)K_1(\gamma a)} \right.$$

$$\left. \left[1 - \frac{I_1(\gamma a)K_1(\gamma b)}{I_1(\gamma b)K_1(\gamma a)}\right]\left[1 - \frac{I_o(\gamma a)K_o(\gamma c)}{I_o(\gamma c)K_o(\gamma a)}\right] \right\}^{1/2} \quad (A.8)$$

Equations A.7 and A.8 take into account the effect of metal fins loading the circuit. Figure A.4 shows that as the radial length of the fin is varied according to the ratio limits 1 < c/a < 2.4, the normalized impedance changes nonlinearly as a function of the dispersion factor.

The equations used to generate the curves shown in Figs. A.3 and A.4 are based on numerous simplifying assumptions. The data points shown in Fig. 7b cannot be superimposed on to these curves. A relationship must be derived which can be used to scale the values of the dispersion factor and normalized impedance in Fig. 7b to the corresponding values in Figs. A.3 and A.4. This will show where the data points in Fig. 7b lie on the overall normalized impedance-dispersion factor curve. To determine such a relationship, a rigorous analysis must be undertaken. This derivation will not be presented here. Instead, the following assumptions and conclusions are made from the above analysis.

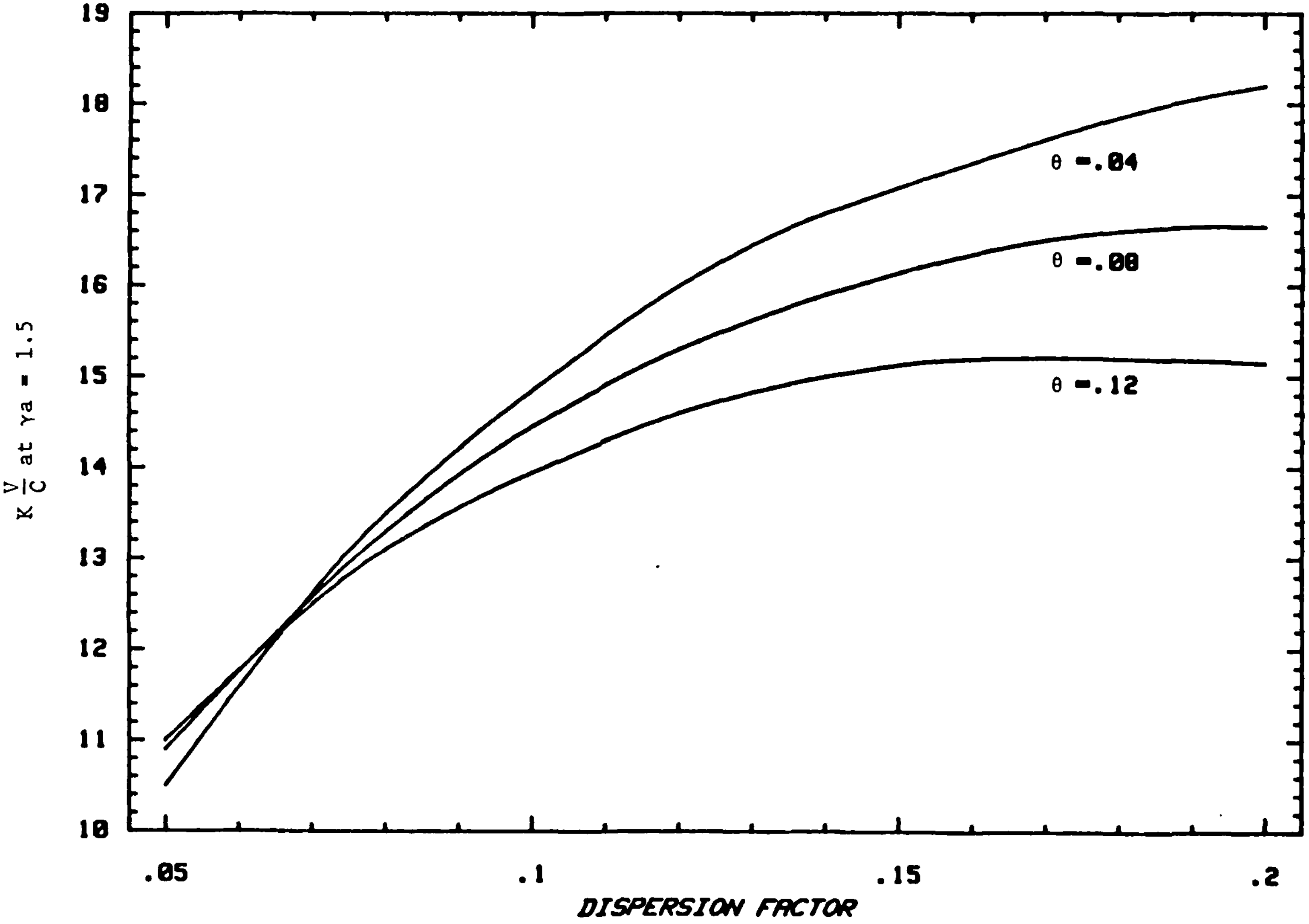

Fig. A.4. Impedance variation versus the dispersion factor (ψ = 0.1, ε_r = 5, N = 3, 1 < c/a < 2.4).

The dispersion factor is a function of the geometrical variations in the loading (metal and dielectric) and the shield-to-helix diameter ratio. Figures A.3 and A.4 illustrate the general effects of varying these parameters on the normalized impedance-dispersion factor relationship. It can be concluded that changing the amount of loading on a helix circuit will result in a nonlinear impedance-dispersion factor variation similar to the curves shown in Figs. A.3 and A.4. In Fig. A.3, a line has been drawn as a linear approximation to the curves. At Df = 0.21, the figure displays an error of roughly 20 percent in this approximation. In Fig. 7b, a 20 percent impedance decrease at Df = 0.21 from a hypothetical line on which the data points lie would represent a rather abrupt impedance deviation. Based on this premise, it is concluded that the normalized impedance-dispersion factor curve which characterizes the data points in Fig. 7b will have a nonlinear variation less than 20 percent at Df = 0.21. Figure A.5 illustrates the sensitivity of the saturation output power to impedance changes in Section 1 for f = 3 GHz. The figure indicates there would be less than a 2 percent decrease in the fundamental output power for a -20 percent impedance deviation. The second harmonic power content becomes very erratic with changes in the impedance. The figure depicts a maximum harmonic power change of 14 percent. Even with this increase, the large signal calculations indicate that the second harmonic is more than 5 db below the fundamental. It is concluded that a linear approximation can be used to extrapolate beyond the data points in Fig. 7b (up through D_f = 0.21). Using an equation of a line simplifies the impedance analysis and still maintains a reasonable accuracy with respect to the large signal calculations.

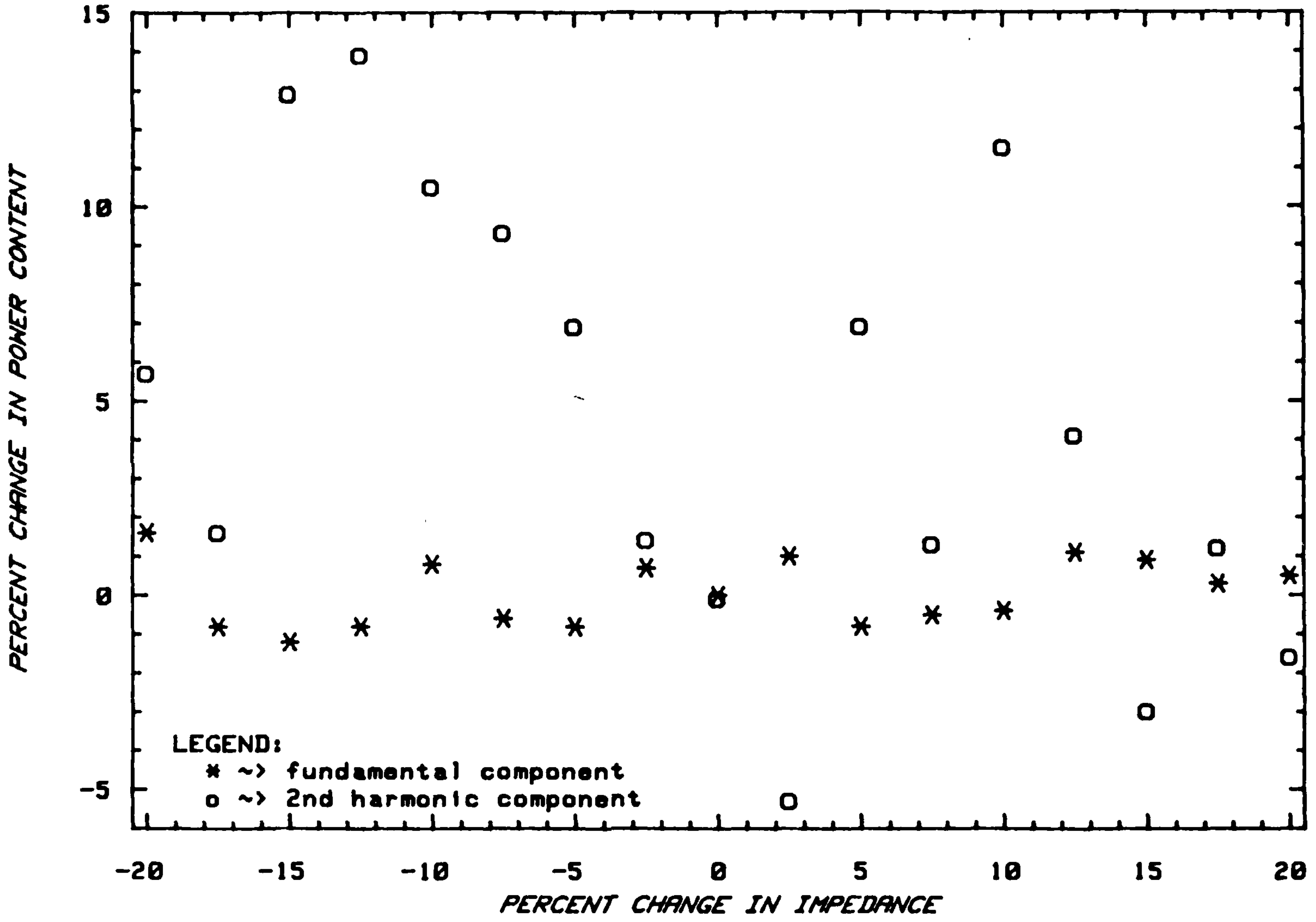

Fig. A.5. Saturation output power sensitivity impedance changes (calculations for F = 3 GHz).

APPENDIX B

LIST OF SYMBOLS

The following list defines those symbols which are commonly used throughout the text, unless the context of a chapter has defined the parameter otherwise.

c	Speed of light
v, v_p, v_o	Cold circuit phase velocity
u_o	Dc beam velocity
f	Fundamental frequency
ω	Angular frequency = $2\pi f$
t	Time
z	Axial tube distance
β	Cold circuit propagation constant = ω/v
β_e	Beam propagation constant = ω/u_o
β_o, k	Free space propagation constant ω/c
Γ	Wave propagation constant in the presence of the beam
C	Gain parameter = $(KI_o/4V_o)^{1/3}$
b	Injection velocity parameter = $\frac{1}{C}\left(\frac{u_o}{v} - 1\right)$
d	Loss parameter
K	Pierce impedance
QC	Space-charge parameter
L1	Length of Section 1 of the output circuit
L2	Length of Section 2 of the output circuit
Lt	Total length of output circuit = $L_1 + L_2$
D_f	Dispersion factor

γ	Radial propagation constant = $\left(\beta^2 - \beta_o^2\right)^{1/2}$
a	Helix average radius
$I_o(\text{arg})$, $I_1(\text{arg})$	Modified Bessel functions of the first kind of order zero and one, respectively
$K_o(\text{arg})$, $K_1(\text{arg})$	Modified Bessel functions of the second kind of order zero and one, respectively
ε	Relative permittivity
ε_o	Permittivity of free space
ε_r	Relative dielectric constant = $\varepsilon/\varepsilon_o$
μ	Permeability
m_e	Mass of an electron
e	Electron charge
F	Force
E	Electric field
θ	Circuit length in radians, $2\pi CN_g$
N_g	Equals the number of undisturbed wavelengths f/c • (total length)

APPENDIX C

TRAJECTORY AND NORMALIZED CURRENT AMPLITUDE PHASE PLOT DEFINITIONS

The purpose of this appendix is to describe the phase plots that are used in Chapter 5 to analyze the RF beam current and circuit field interaction. Figures C.2, C.3, and C.4 are examples of these plots which display the electron bunching phenomena and normalized beam current amplitude with respect to the circuit field regions and axial distance.

The fundamental and second harmonic components of the circuit field can be visualized by comparing Fig. C.1 with Figs. C.2, C.3, and C.4. The second harmonic circuit field has a periodicity of two times that of the fundamental. The force on an electron due to the circuit field can be written as F = - e E, so that a region of positive circuit field labeled D represents the region where the electrons are decelerated by the circuit field. In the circuit field regions labeled A, the axially directed electric field is negative, so the electrons become accelerated in the positive z direction. Referring to Figs. C.2, C.3, and C.4, the accelerating and decelerating circuit field regions are labeled corresponding to the regions indicated in Fig. C.1. The fundamental RF circuit field regions are indicated by the dashed lines, which occur every π radians in fundamental phase. The fundamental regions are labeled at the top of the plot. The second harmonic RF circuit field regions are indicated by the starred lines, and occur every π radians in second harmonic phase. The second harmonic regions are labeled at the

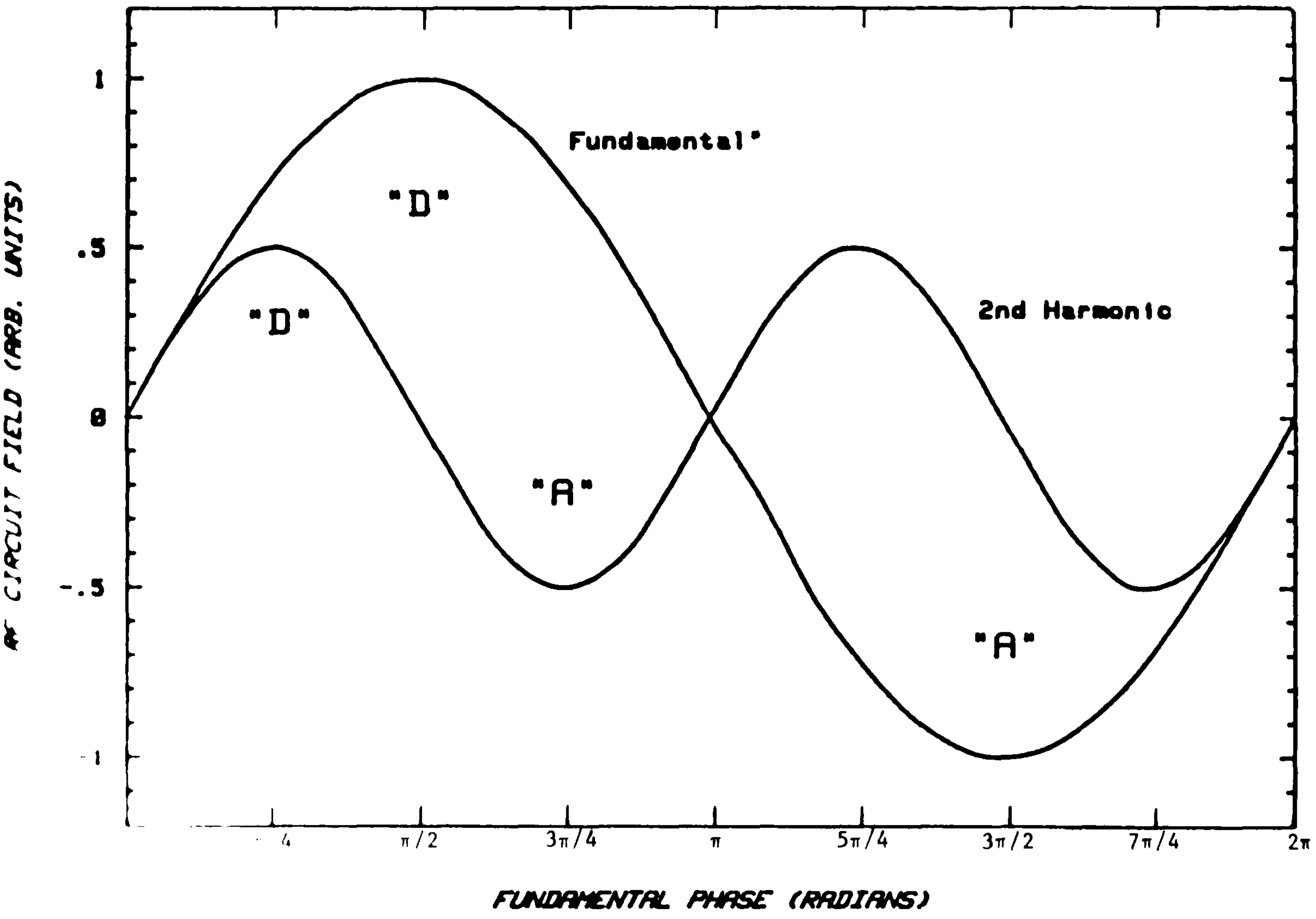

Fig. C.1. RF circuit field model.

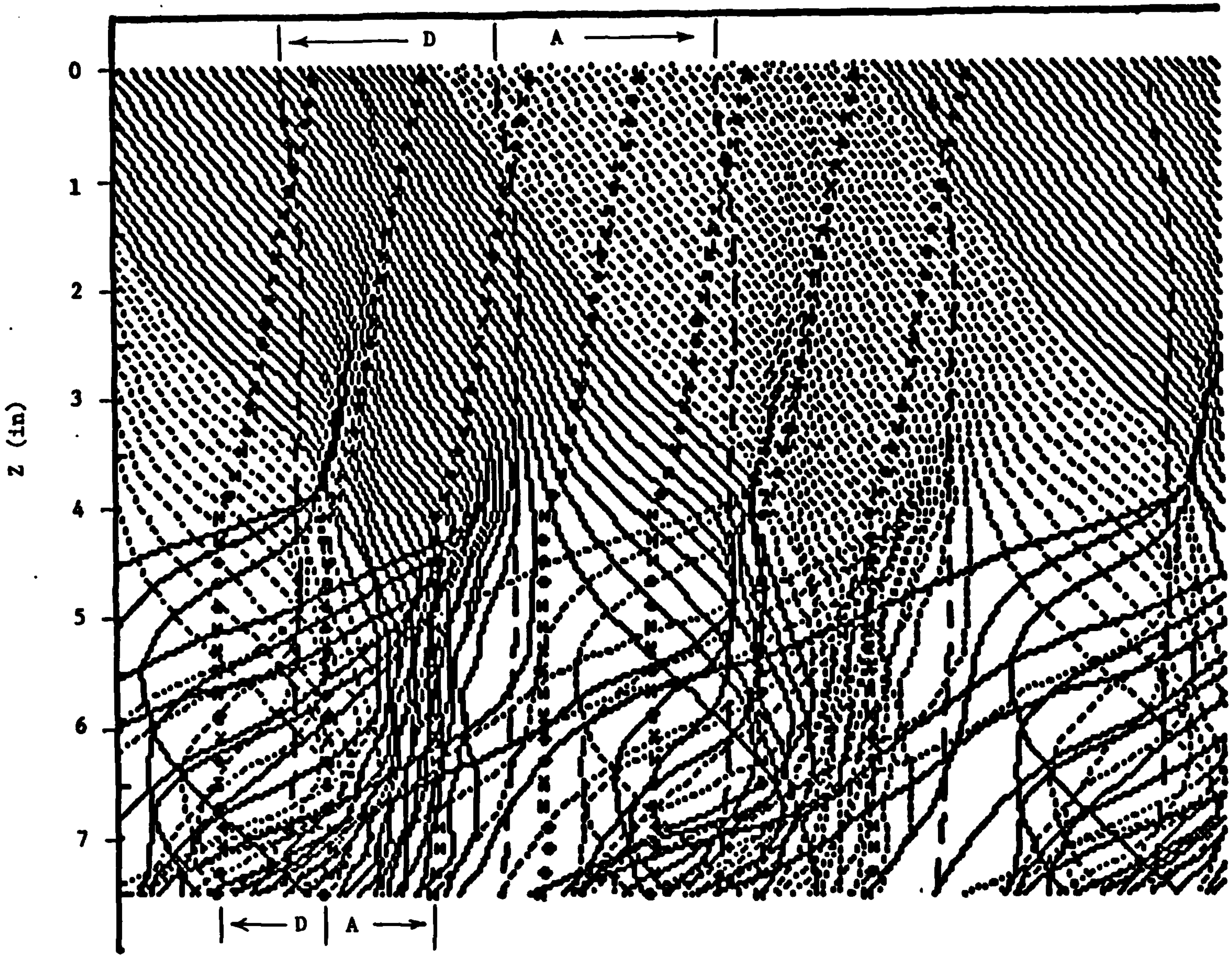

Fig. C.2. Phase trajectory versus output circuit length.

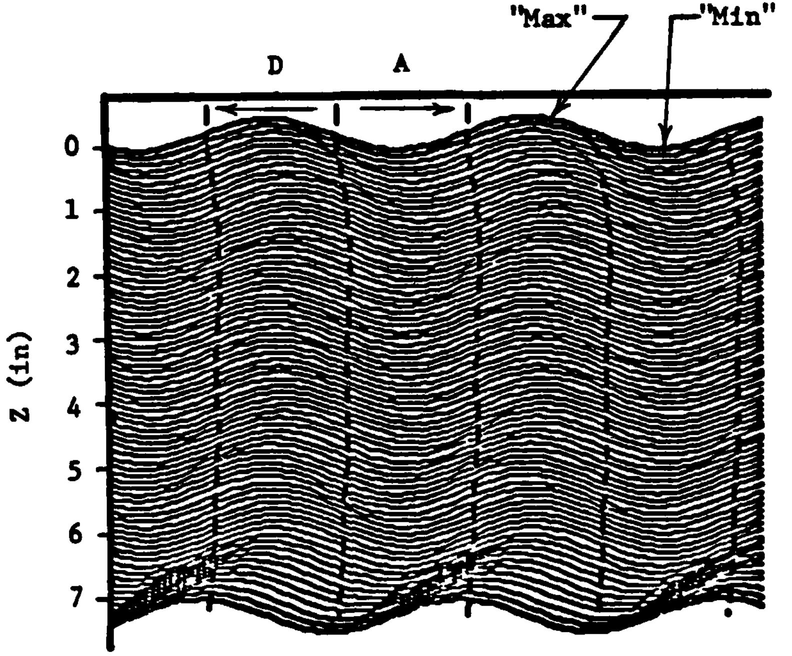

Fig. C.3. Normalized current amplitude versus output circuit length (fundamental).

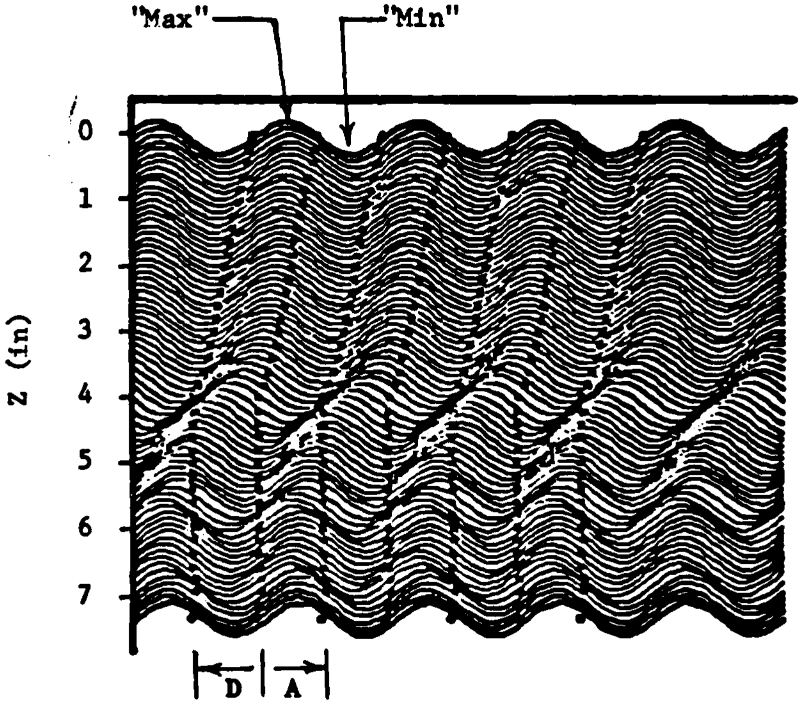

Fig. C.4. Normalized current amplitude versus output circuit length (2nd harmonic).

bottom of the plot. The dashed and starred lines represent contours of zero force. The information in each plot repeats every 2π radians.

In order to obtain a high level of saturation efficiency, the electrons must travel in the decelerating circuit field region of the fundamental frequency component. At the input of the tube, the electrons are distributed uniformly with respect to a complete cycle of the circuit field. The electrons in the negative field region will accelerate forward into a positive field region. The electrons in the positive field region will lose energy to the circuit field and decelerate out of the positive field region. Amplification of the circuit wave occurs when the accelerated electrons from the negative field region bunch with the electrons in the positive (or decelerating) field region. The magnitude of the amplification depends on the tightness of the electron bunch, and the duration the bunch remains within the decelerating circuit field region.

In Fig. C.2, the concentration of the electron trajectory curves indicates electron bunching, and is proportional to the charge density distribution in the beam. Figures C.3 and C.4 illustrate the normalized RF beam current amplitude with respect to the circuit field and the output circuit length. The current amplitude has been normalized to constant values for the maximum and minimum, as shown in the plots. This enables the amplitude to be easily determined within any field region and at any axial position. Figure C.3 depicts the RF beam current for the fundamental frequency component. Figure C.4 displays the second harmonic frequency component of the current. The maximum amplitude is indicated by the label "max," and conversely the minimum is labeled by "min."

The circuit field location and axial position of the fundamental and second harmonic components of the current (Figs. C.2 and C.3) are directly related to the field location and axial position of the electron bunching displayed in Fig. C.2. Regions of electron trajectory concentrations (bunching) correspond to peak RF current amplitudes.

MISSION
of
Rome Air Development Center

RADC plans and executes research, development, test and selected acquisition programs in support of Command, Control Communications and Intelligence (C^3I) activities. Technical and engineering support within areas of technical competence is provided to ESD Program Offices (POs) and other ESD elements. The principal technical mission areas are communications, electromagnetic guidance and control, surveillance of ground and aerospace objects, intelligence data collection and handling, information system technology, ionospheric propagation, solid state sciences, microwave physics and electronic reliability, maintainability and compatibility.